# Cleavage fracture during multiaxial loading: identifying stress parameters in ferritic steels

by

Thijn van Zelst

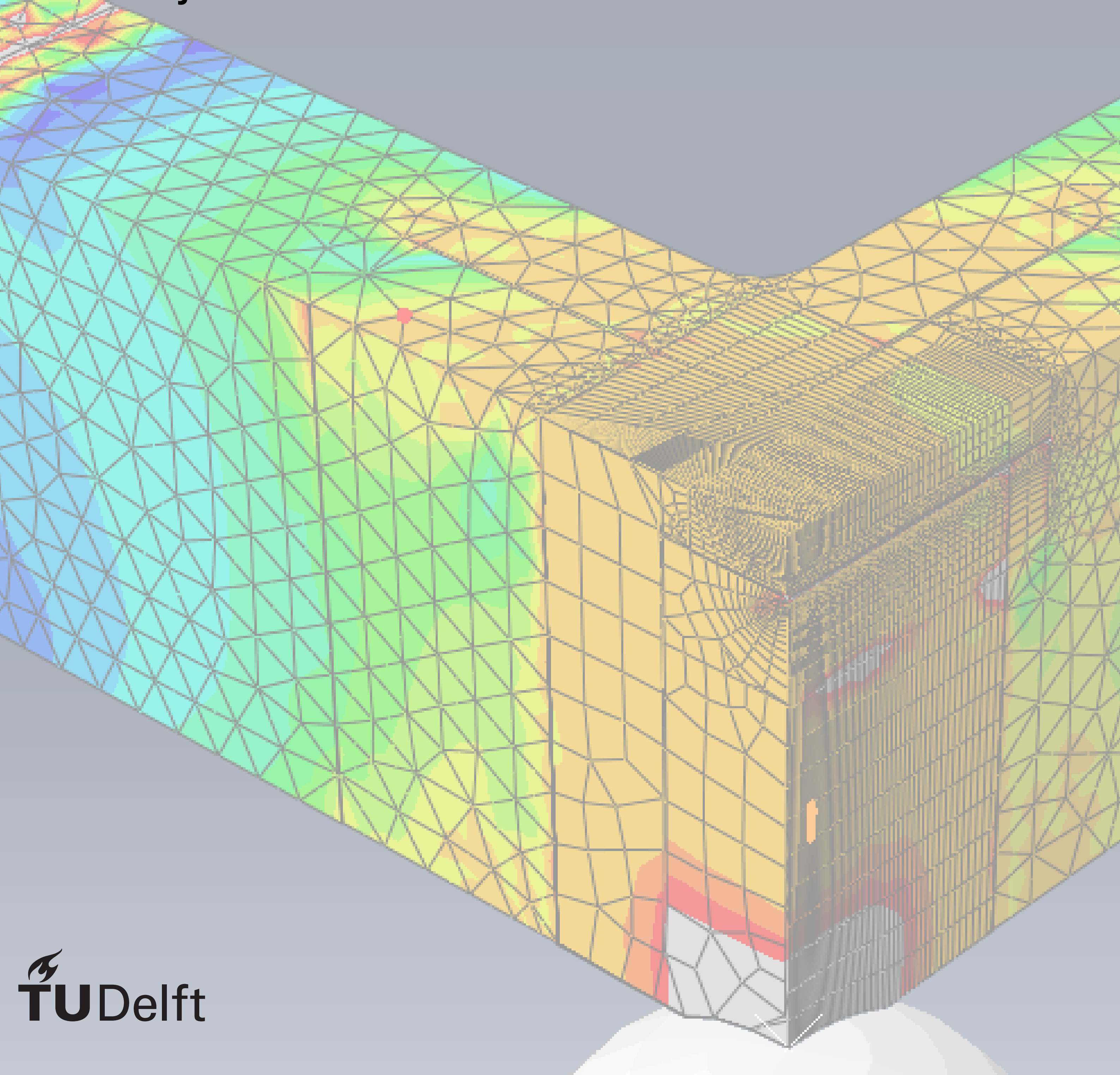

# Cleavage fracture during multiaxial loading: identifying stress parameters in ferritic steels

by


# Thijn van Zelst


to obtain the degree of Master of Science
at the Delft University of Technology,
to be defended publicly on Wednesday, the 28th of October, 2020 at 9:00.


**Abstract**

Brittle fracture in ferritic steels is a field in which a lot of research has been performed over the years. Most of this research has been done on uniaxially loaded specimens, such as single edge notched bend specimens. From these experiments, the maximum principal stress criterion is used in the Weibull distribution method as proposed by Beremin, and is observed to accurately predict the fracture toughness distribution. However, when multiaxial specimens are considered, the maximum principal stress criterion no longer accurately predicts the fracture toughness distribution. In this thesis, other failure criteria than the standard maximum principal stress are considered as a solution to this problem. Using the data provided in the 2006 paper "An Experimental Investigation of the Effect of Biaxial Loading on the Master Curve Transition Temperature in RPV Steels" by R. Link, A Joyce and C. Roe, the properties of Shoreham pressure vessel steel are obtained. Furthermore, the fracture toughness from the tested cruciform specimens allows for the reconstruction of the stress state around the crack tip during fracture. This is done by creating various cruciform specimens in the Abaqus finite element analysis program, which are loaded in accordance with the paper. The resulting stress state is used in the calibration of the Weibull parameters in the Weibull distribution. It was found that uniaxially loaded specimens show good agreement with the predicted failure probabilities. Additionally, it was confirmed that the biaxially loaded specimens do not show good agreement when the maximum principal stress is the failure criterion. When the failure criterion is altered so that only microcracks that do not experience large triaxiality contribute to fracture, good agreement is obtained for both the uniaxially and biaxially loaded specimens. Hence, it is found that triaxiality is very important for cleavage fracture, with high levels of triaxiality preventing microcracks from propagating. This leads to a proposed failure criterion where the maximum principal stress criterion is applied, and only elements that do not experience high levels of triaxiality contribute. It is suggested to further test these conclusions under a variety of loading conditions, for which an alternate specimen is proposed.


| | | |
|---|---|---|
| Student number: | 4285689 | |
| Project duration: | December 1, 2019 – October 28, 2020 | |
| Thesis committee: | Dr. C. L. Walters, | TU Delft, supervisor |
| | Dr. V. Popovich, | TU Delft |
| | Ir. Q. Jiang, | TU Delft |


An electronic version of this thesis is available at `http://repository.tudelft.nl/`.


TU Delft

# Preface

This thesis, "An investigation into possible representative stress parameters for the determination of the Weibull distribution of brittle ferritic steels", and currently in your hands, is written to further the understanding of the effect multiaxial loading on the fracture toughness. Finishing of this thesis marks the end of my time at the University of Delft as a student, as it has been written to fulfill the graduation requirements of the Materials Science department in the 3ME faculty. For me, this work was not just another project, but also an exercise in responsibility and endurance; the thesis as it lies before you is significantly different in scope than initially expected, with no experimental work being possible due to Covid-19. While this is the case, I have been successful in changing course, and with this thesis, I hope to answer how fracture toughness can better be described when loaded biaxially.

Finishing this thesis would not have been possible without the excellent support of my daily supervisors C.L. Walters and Q. Jiang, and the discussion and guidance they provided. The support provided by V. Popovich on this thesis is also very much appreciated. Additionally, I'd like to thank R. Link and J. Joyce, with whom I cooperated to obtain the results from their paper, without which the change in course would not have been successful. For their help I'm truly grateful.

Of course, I've been supported during this thesis and during all the other years at the university by many people. I'd like to thank my parents and sister, for their support and understanding, no matter the circumstances. I'd also like to thank the rest of my family, who were always available when needed. Additionally, I'd like to thank: My roommates, whose support works in mysterious ways; My dear friends, who helped maintain my morale during these long months; The gears, for whom osmium will always be the best metal (I'm sorry, no osmium in this thesis), and who put me on the path of becoming a materials engineer.

I hope you enjoy reading this thesis, and you learn something you did not know before!

Thijn van Zelst,

Delft, 15$^{\text{th}}$ of October, 2020

# Contents

# 1
# Introduction

Failure of metals is a broad subject with many researchers attempting to accurately predict failure under a variety of circumstances. If the metal is very brittle or the load is applied very quickly, the metal can experience 'cleavage fracture', which is a transgranular fracture that occurs along crystallographic planes such as the {100} plane in ferritic steel [11]. An example of transgranular cleavage fracture is shown in Figure 1.1. In cleavage fracture, the distribution of certain flaws at the granular level starts to become more important, with the start of crack growth from such a flaw being the critical step in the cleavage process. The applied stress intensity is no longer an accurate measure that can be used to determine when fracture will occur. Since the orientation of grains and the distribution of flaws in the microstructure is random, the metal will start to fail according to a failure probability which depends on the microstructure and the stress state in this microstructure, also called the local stress state. A theory that makes assumptions about the microstructure and then uses the local stress state to predict cleavage fracture is called a local approach.

There are a number of local approaches that try to describe this kind of failure, with one of these theories being the Beremin model [9]. The Beremin model describes the probability of failure using a function of the first principal stress. Other authors [66][31] have modified this statistical model by introducing stress parameters other than the first principal stress into the same function. Since there is not yet consensus on how the local stress state in a metal affects fracture, investigating the local stress parameter is worthwhile.

This thesis aims to find a local stress parameter such that the Beremin model accurately predicts the failure distribution for multiaxially loaded structures. These predictions can then be used to design structures that are less prone to cleavage fracture. An example is a pressure vessel in a nuclear reactor. First the need for an accurate model is discussed, after which the theoretical background of the thesis is discussed and a research question is formulated. The following chapters describe the modelling process and the obtained results. Finally, the results are evaluated and the research question is answered.

## 1.1. Predicting cleavage fracture

There has been an increase in demand in recent years for more accurate analysis of the structural integrity and fitness-for-service of structures such as storage tanks and nuclear reactor pressure vessels [49]. A more accurate analysis of these structures means that better decisions can be made when these structures are repaired or when to replace them. In general, these decisions are based on fracture mechanics based approaches, called engineering critical assessment (ECA) procedures [34] , which cover a variety of methods to determine the structural integrity of structures. It was noted by Ruggieri and Dodds [49] that the cleavage predictions as produced by the ECA procedures rely on macroscopic measurements of the fracture toughness from conventional specimens. These conventional specimens are limited in scope and are not always equivalent to more complex structures.

Transgranular cleavage itself is one of the most serious failure modes in ferritic steels [1] and can be described with the ECA approaches. If a crack is present, the stress intensity around its tip can trigger transgranular fracture, while the stresses in the structure are far below the yield stress. This fracture then leads to catastrophic failure of the structure, due to the crack propagating in an unstable manner.

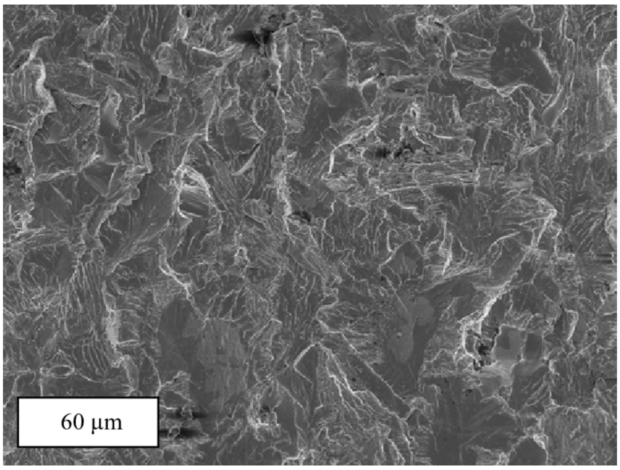


Figure 1.1: An example of transgranular cleavage fracture [54].

The ECA approach uses measurements of the cleavage fracture toughness to determine which flaws are acceptable and do not require repair. To measure the fracture toughness, the critical strain energy release rate $J_c$ or the crack tip opening displacement has to be derived from fracture specimens. The critical strain energy release rate is best understood as the decrease in the total potential energy as a function of the surface area of the crack, while the crack tip opening displacement is used as a measure of the stress state around the crack tip during fracture and thus as a measure of the stress intensity factor and the energy release rate. The conventional fracture specimens used to determine the fracture toughness are the single edge notch bend (SENB) and compact tension (CT) specimens, which are fractured under small scale yielding conditions for ECA methodologies. However, these ECA procedures are limited in scope and do not show the observed strong sensitivity of fracture to the microstructure of metals [49]. The ECA procedures also have a limited ability to predict the effect of different constraint conditions. For example, if a crack is shallow, the crack is more likely to propagate in a ductile manner, while if the crack is deep, the crack is more likely to propagate in a brittle manner. This means that there is an effect of depth and geometry on the stress state in front of the crack tip, which is commonly called constraint.

The limitation of the ECA procedures caused a significant interest in the prediction of cleavage fracture for a variety of crack configurations and different loading modes, to describe cleavage fracture using a micromechanical model. Based on this interest the Beremin model was developed by the French Beremin group [9][2]. It is a well known model, and is used to describe brittle fracture behaviour of ferritic steels [2]. It is based on a micromechanical model that relies on cracked carbides to form directly after yielding occurs. How these cracked carbides look like can be seen in Figure 1.2. They act as Griffith microcracks, i.e. the presence of these microcracks causes the observed fracture strength to be lower than the theoretical fracture strength, which is described by Griffith as the maximum possible stress a solid can withstand when a crack is present with no surrounding flaws. The propagation of a Griffith microcrack is then described by Griffith's criterion [21].

The Beremin model then assumes that for a certain stress around the crack tip, there is a probability based on amount of microcracks present in the metal and the stress state around the crack tip. This stress state is defined by Beremin as the Weibull stress and is assumed to be the maximum principal stress. The maximum principal stress being the opening mode stress, the most critical stress, this assumption is reasonable.

This assumption is questioned in the work of Bass [66], where an effect of multiaxial loading is observed. In his work a variety of stress states are considered that can act as the stress state used by the Beremin model. It was found that of the stress parameters considered, only the Hydrostatic stress criterion was able to predict the effect of biaxial loading on a specimen.

The observations of Link and Joyce [27] disagree with the conclusion of Bass and his co-workers, with no effect of biaxiality being shown for a variety of specimens, albeit not using the model proposed by Beremin

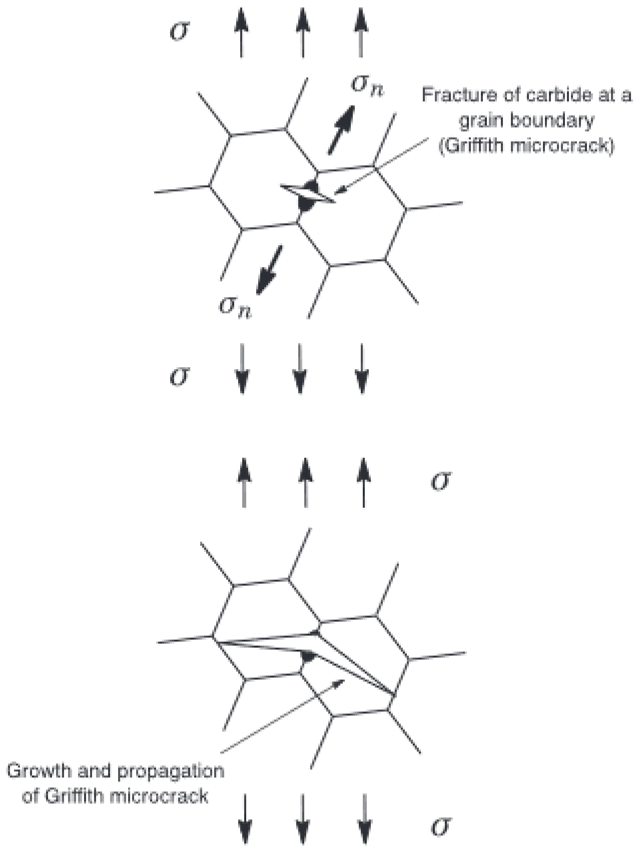


Figure 1.2: Depiction of carbide crack nucleation under stress, with transgranular crack propagation [49]

but the master curve method [31]. They used the work of Oak Ridge National laboratory [66][6] (ORNL) as a basis to continue working, but also used data from the European forging steel Round Robin [22][68] and their own data from cruciform specimens of Shoreham pressure vessel steel[31]. They conclude that there is no effect of biaxial loading on the reference temperature $T_0$, which is defined as the temperature where the median fracture toughness is 100 MPa$\sqrt{m}$ in a 25 mm thick specimen. This reference temperature can then be used to determine the median fracture toughness. Since the biaxial effect is not observed using this approach the paper is contradictory with Bass's results [66], and thus it is clear there was no concensus at the time.

Ostby [44] identified the need for a cleavage fracture assessment procedure that takes biaxial loading into account. The effect of biaxial loading is small in the case of small scale yielding and larger for large scale yielding. It is observed that the most important effect of biaxial loading is an increase of the crack driving force as a function of the applied strain, with biaxial loading causing the strain capacity of the large specimen to be significantly decreased.

Theiss [56] indicates that shallow-flaw specimens placed under biaxial loading experience a toughness reduction compared to similar specimens placed under uniaxial loading. This was tested using a cruciform specimen, which showed that the fracture loads for either uniaxial or biaxial loading were roughly the same. However, the uniaxial specimen withstood significantly more deformation at failure than the biaxial specimen.

More recently, Meek [41] explores the assumption of high constraint specimens finding overestimating values for the fracture toughness. It is mentioned that biaxial loading can cause the force acting on the crack tip to be overestimated, leading to a loss of conservatism; The measurements indicate that failure occurs earlier than predicted. If the force acting on the crack tip is lower, the fracture toughness will be higher. This is not in line with the results from Bass's paper [66], where biaxial loading leads to reduced fracture toughness. However, in experimental tests considered by Meek [41], the effect of in-plane biaxial loading is not consistent and has been shown to decrease crack growth resistance, to increase fracture toughness and to increase fracture resistance. However, in the case of out-of-plane loading, an increase in crack-tip constraint and a reduction in fracture toughness os observed. This observation does match the results as shown by Bass [66]. Two causes for this difference in response are mentioned. One cause is the different effect of biaxial loading on the crack driving force and the fracture toughness, with the response depending on the parameter that dominates. The other is that the effect of biaxial load depends on the type of fracture that occurs, as the effect of constraint on the fracture toughness changes if the type of fracture changes.

## 1.2. Research question

As shown in the previous section, there is a clear gap in the literature concerning the effect of constraint on the stress criterion used to determine fracture toughness. It is also identified that there is a need for a stress criterion that accurately depicts the effect of the stress state on the fracture of structures, most often used to determine proper procedures for cracks in the pressure vessels of nuclear reactors. To that end the following research question is used in this thesis: *"What is a representative stress parameter that can be used to determine the distribution of the cleavage fracture toughness of ferritic steels under varying levels of constraint and multiaxial loads?"*

In order to find an answer to this question, several subquestions have to be answered:

1. How can cleavage fracture toughness in ferritic steels be quantified?
2. What is the effect of constraint on fracture and how is this effect quantified?
3. Which method is best used to determine the distribution of the cleavage fracture toughness?
4. Which possible representative stress parameters should be considered?
5. Is the model that is found representative for a structure in the real world?

The hypothesis for the main research question, based on the evidence provided by Bass's papers [66] [6] and other papers [68][44][41], is that the hydrostatic fracture criteria captures the effect of multiaxiality on the fracture toughness of the specimens in the cases of biaxial loading, while the maximum principal stress criteria only captures the effect of uniaxial loading. Thus, by looking at the difference in failure distributions between cruciform specimens that have been loaded differently, the effect of multiaxiality and constraint can best be explained by the hydrostatic stress criteria as proposed in the work of Bass [66].

# 2

# Theoretical background information

To answer the research question, it is important to understand how cleavage fracture is predicted and which failure criteria are considered as the stress parameter in the literature. In this chapter the theoretical background of cleavage fracture is discussed, as well as the effect of constraint and triaxiality.

## 2.1. Local approaches to cleavage fracture

Most methods to describe the cleavage fracture using a probabilistic model have been greatly influenced by the work of Weibull [63]. In his work, the effect of the size of microcracks on fracture strength of brittle materials with a macroscopic crack is described with the weakest link approach. These microcracks are randomly distributed, and propagation of these microcracks obeys the Griffith criterion. The assumption is made that the microcrack starts propagating only when the stress normal to the plane of the flaw is high enough. This critical stress is called $\sigma_c$ and depends on the size of the microcrack $l_0$, the surface energy $\gamma$, which can be described as the work required to create a certain area of fracture surface, the Young's modulus E and the Poisson's ratio $\upsilon$, which are included in the following alteration of the Griffith equation [21]:

$$\sigma_c = \sqrt{\frac{2E\gamma}{\pi(1-\upsilon^2)l_0}} \tag{2.1}$$

This equation can then be used to find if the crack will start propagating into the surrounding grains, based on the energy balance in the structure. In this case, the stress ahead of the larger crack is considered to be the far field stress of the microcracks. These microcracks then propagate when the critical stress, as predicted by the Griffith equation, is reached. The Griffith criterion can be satisfied by small particles for ferritic steels with a size that is in the order of micrometers.[1]. However, this equation is impractical due to the required knowledge of the surface energy $\gamma$, as well as the size and orientation of the microcracks.

Because of this, mathematical models of cleavage fracture were considered. This was pioneered in the works of Epstein [15] and later expanded by Freudenthal [18]. In these works, it was shown that the failure distribution depends on how the fracture resistance of randomly distributed Griffith microcracks is described. This approach is called the elemental strength approach [16]. It aims to characterize the stress state for which the Griffith cleavage condition is met. This is explored extensively in the work of Epstein [15], Argon and McClintock [38] and Batdorf and Crose [7].

The Weibull approach served as inspiration in the work of Freudenthal [18], where the statistical distribution of the microcrack size and the fracture distribution are found to be connected. This is further expanded in the work of Evans [16] and Ritchie, Knott and Rice [48]. In this work, Ritchie et al. assumed a different weakest link model, with the propagation of a crack across grain boundaries being the weakest link. This means that the critical stress must extend over a certain distance in front of the crack tip, before cleavage fracture can occur. However, further investigations [23] [13] [62], found no such relationship between grain size and distance.

Later statistical models used the start of cleavage in hard particles as the weakest link, which is supported by experimental results in the work of Low [33] , Owen et al. [45] and McMahon and Cohen [39]. In these experiments, it was found that Griffith microcracks form due to local plasticity, and thus, local yielding. Based on these experimental results and knowledge of the work of Ritchie et al. [48], it is then assumed that the weakest link is the propagation of the microcrack. This is the approach the Beremin group used [9].

In this approach, it is assumed that the stress parallel to the grain boundary affects the carbide and causes these microcracks to propagate into the grains. Since the distribution of carbides and grains is random, the probability of a volume experiencing fracture depends on the location and orientation of the largest flaws. Additionally, it is assumed that failure of elements that do not have a shared volume are independent. Furthermore, the probability of failure for an element is assumed to be proportional to the volume of the element. Then, by using the probability theory, the failure probability of this volume, $\delta$P, can be determined:

$$\delta P = \delta V \int_{a_c}^{\infty} g(a)da, \tag{2.2}$$

where $g(a)$ is a function that determines the probability of finding a microcrack of a certain size, at least larger than the critical size $a_c$, for which the crack will propagate in an unstable manner [29].

To extend this theorem to the micromechanical level, the function $g(a)da$ is approximated using the form $g(a) = (\frac{1}{V_0})(\frac{\zeta_0}{a})^{\zeta}$, where $V_0$ is the reference volume [16] and $\zeta$ is a parameter of the distribution of flaws. It should be noted that the reference volume can be chosen arbitrarily, as long as the reference volume is small enough that the original assumption is valid; the failures of elements that do not have a shared volume, are independent.

Additionally, it is possible to find a relationship between the stress state ($\sigma_{eq}$) around the flaw and its critical size, $a_c = K_{Ic}^2/(Y\sigma_{eq}^2)$ [1]. Here $K_{Ic}$ is the local fracture toughness of the material that is considered, in this case a ferritic steel. The Y depends on the geometry of the specimen. Here an important assumption is made; $\sigma_{eq}$ is the tensile stress that acts on the flaw in Mode 1, i.e. the tensile stress opens the crack further, similar to what is shown in Figure 1.2. This means that the maximum principal stress is considered as the $\sigma_{eq}$, due to the random distribution of flaws leading to a large probability that this is the maximum opening stress acting on the flaw.

Combining these relationships with each other and then inserting them in equation 2.2, the failure probability for a certain volume with a crack already present then becomes:

$$P_f(\sigma_1) = 1 - exp[-\frac{1}{V_0}\int_{\Omega}(\frac{\sigma_1}{\sigma_u})^m dV], \tag{2.3}$$

where $\Omega$ is the volume near the crack tip that experiences a certain stress state or plastic strain, for example, the area where the von Mises stress exceeds the yield strength. Beremin simplified this equation by splitting the above equation as follows:

$$P_f(\sigma_1) = 1 - exp[(\frac{\sigma_w}{\sigma_u})^m], \tag{2.4}$$

where $\sigma_W$ is called the Weibull stress and is defined as follows:

$$\sigma_W = [-\frac{1}{V_0}\int_{\Omega}\sigma_1^m d\Omega]^{\frac{1}{m}}, \tag{2.5}$$

In this model, $m$ is the shape parameter which defines the slope of the failure probability curve and $\sigma_u$ is the measure of the $63^{rd}$ percentile Weibull stress around the crack tip. The parameter $m$ and $\sigma_u$ are considered material parameters and constant, but this depends on the assumption that all micro-cracks form immediately at the onset of plastic deformation. In a two-parameter Weibull distribution, only the $m$ and $\sigma_u$ are used to determine the fracture distribution. However, it is possible that a two parameter Weibull distribution does not match the failure probability, as observed in the work of low [33]. This lies in the property of equation 2.4, as long as the $\sigma_w$ is not equal to 0, there is a possibility for fracture to occur. It has been shown that a critical stress must be reached before failure can start to occur [33], also called the $\sigma_{c,min}$. This means that the two-parameter Weibull distribution in some cases produces inaccurate results. When this critical stress is included, the original two-parameter Weibull distribution becomes a three-parameter Weibull distribution:

$$P_f(\sigma_1) = 1 - exp[(\frac{\sigma_w - \sigma_{c,min}}{\sigma_u - \sigma_{c,min}})^m], \tag{2.6}$$

where the $\sigma_{w,min}$ is used to ensure that fracture does not occur before a certain stress. The value of $\sigma_{w,min}$ is thickness independent. This means that three-parameter Weibull distributions will show a more accurate distribution if the Weibull parameters are properly calibrated.

Now that the failure distribution has been more closely examined, the stress parameter $\sigma_1$ is considered. The $\sigma_1$ is the stress parameter considered in the work of Beremin [9], and is widely known as the first principal stress criteria. For standard test configurations, such as the single edge notched bend specimens, the maximum principal stress criteria accurately matches the results produced using the Beremin model [9]. As discussed in the introduction, the assumption that the maximum principal stress criterion is sufficient under any type of loading is questioned. Hence, a new stress parameter $\sigma_q$ is introduced in this thesis, which replaces the $\sigma_1$.

To understand how the $\sigma_q$ should function under a variety of loading conditions, the stress state around the crack tip should be considered. The Weibull stress is based on critical stresses in front of the crack tip, in this thesis approximated using $\sigma_q$, and the volume of the metal that has plastically deformed. As such, it is determined by taking the integral of the stresses over the region that has been plastically deformed, with the example given for a cylindrical volume in equation 2.7. Here, the l is the length of between the origin and the location of interest, $\phi$ is the angle between the origin and the location of interest and z is the height of the location of interest in the cylinder. Other coordinate systems can be implemented as well, depending on what kind of crack has to be analysed. For example, in Bass's paper a spherical volume is considered [66].

$$\sigma_w = [\frac{1}{4\pi V_0}\int_0^z\int_0^{2\pi}\int_0^l \sigma_q^m sin\phi \, dl \, d\phi \, dz]^{\frac{1}{m}}. \tag{2.7}$$

As shown by Beremin and others, the maximum principal stress is generally considered to give good results [9][17]. However, it was found by Bass et al. that the maximum principal stress was not able to predict the biaxial effect as observed for cruciform specimens [66]. To improve upon the maximum principal stress criterion, several proposals are made in Bass's paper [66]:

- Maximum principal stress [66]:
$$\sigma_q = max(\sigma_1, \sigma_2, \sigma_3) \tag{2.8}$$
- Normal stress averaging [66]:
$$\sigma_q = \sigma_n \tag{2.9}$$
- Principle of independent action [14]:
$$\sigma_q = (<\sigma_1>^m + <\sigma_2>^m + <\sigma_3>^m)^{\frac{1}{m}} \tag{2.10}$$
- Coplanar energy release rate [66]:
$$\sigma_q = (\sigma_n^2 + \frac{4\tau^2}{(2-\upsilon)^2})^{\frac{1}{2}} \tag{2.11}$$
- Noncoplanar energy release rate [24][28]:
$$(\sigma_n^4 + 6\sigma_n^2\tau^2 + \tau^4)^{\frac{1}{4}} \tag{2.12}$$
- Hydrostatic stress [66]:
$$\sigma_q = \frac{\sigma_1 + \sigma_2 + \sigma_3}{3} \tag{2.13}$$

In these equations, the stresses $\sigma_1$, $\sigma_2$ and $\sigma_3$ are the three principal stresses, while $\sigma_n$ and $\tau$ are the normal stress and shear stress respectively. The normal stress and shear stress are determined using:

- Normal stress:
$$\sigma_n = \sigma_3 sin^2\phi cos^2\theta + \sigma_2 sin^2\phi sin^2\theta + \sigma_1 cos^2\phi \tag{2.14}$$
- Shear stress:
$$\tau^2 = \sigma_3^2 sin^2\phi cos^2\theta + +\sigma_2^2 sin^2\phi sin^2\theta + \sigma_1^2 cos^2\phi - \sigma_n^2 \tag{2.15}$$

Here, $\phi$ is the angle between the volume that is considered and the crack tip, while the $\theta$ is the angle of the stress field in front of the crack tip and the microcrack in the volume element.

Other failure criteria than the ones described in Bass's paper can be used; In Bass's paper [66] it is mentioned that only the hydrostatic stress criterion captures the biaxial effect, while the other proposed failure criteria do not do so. Hence, it is useful to find other failure criteria that can capture the biaxial effect. Apart from the biaxial effect, the paper by Yin et al. [68] indicates that there is also an effect of the depth of the crack. This means the proposed failure criterion must function for a variety of conditions, all of which affect the level of constraint close to the crack tip. However, what exactly constraint is and how the level of constraint can be determined differs from experiment to experiment. To that end, it is important to have a definition of what constraint is and which parameters of experiments have an effect on constraint. Additionally, it is important to know what sort of effect the multiaxial loading has on the stress state in front of the crack tip.

## 2.2. The effect of multiaxial loading

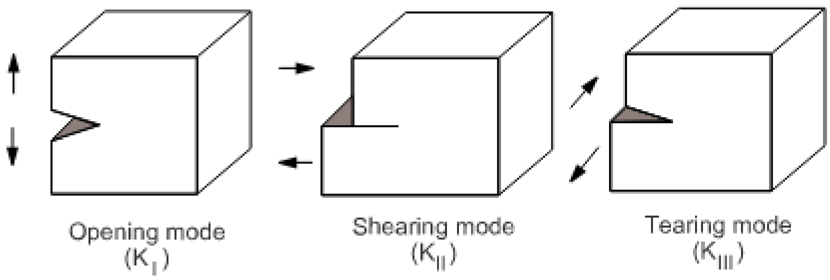


Figure 2.1: The three fundamental opening modes[58]

To understand how the stress state affects cleavage fracture and why Beremin has chosen the maximum principal stress as the parameter to determine the Weibull stress, it is important to consider the three different crack propagation modes that exist. These are shown in Figure 2.1. As mentioned earlier, only mode I is generally considered as the most important fracture mode, since it is the most critical failure mode and thus also occurs the most. It is called the opening mode, as can be seen in the figure. This is because only for mode I the crack opens, while mode II and mode III only occur under shear. As a result, the crack does not open significantly in mode II and III. The applied loading determines which mode will occur, as the orientation of the crack in relation to the stresses around its crack tip determine which mode will occur. For commonly used fracture experiments, the maximum principal stress lies perpendicular to the crack, which means that these experiments will be loaded in mode. It should be noted that for each of these modes, the stress intensity $K$ has been derived, with the most common one being $K_{Ic}$. The subscript $I$ in $K_{Ic}$ denotes the considered mode and the subscript $c$ means that it is the critical value for which propagation will occur. The basis of $K_I$ lies in the Westergaard solution [64], which shows the stresses around the crack tip as a function of the stress intensity, the distance to the crack tip and the angle of the crack relative to the applied stresses. However, the $K$ value is only valid in the elastic region, or when the area of plasticity is small. The Westergaard solution is not able to describe the stresses in a plasticly deformed region and since the cracks discussed in this thesis have large plastic deformation around the crack tip, the Westergaard solution can not be used. Instead, another way to characterize the fracture must be used. However, the fracture toughness of both Bass et al. [66] and Link et al. [31] are presented with stress intensity factors, and should thus satisfy the Westergaard solutions. It should be noted that this is not the case, with the reported stress intensity factors being determined by the following relation instead:

$$K_J^2 = JE/(1-\nu^2), \tag{2.16}$$

where $J$ is the critical value for the energy release rate, $E$ is the Young's modulus and $\nu$ is the Poisson's ratio.

The actual measure of the fracture toughness used in Bass's [66] and Link's [31] paper, as well as this thesis, is the J-integral, which measures the energy release rate around the crack tip, by means of a contour integral

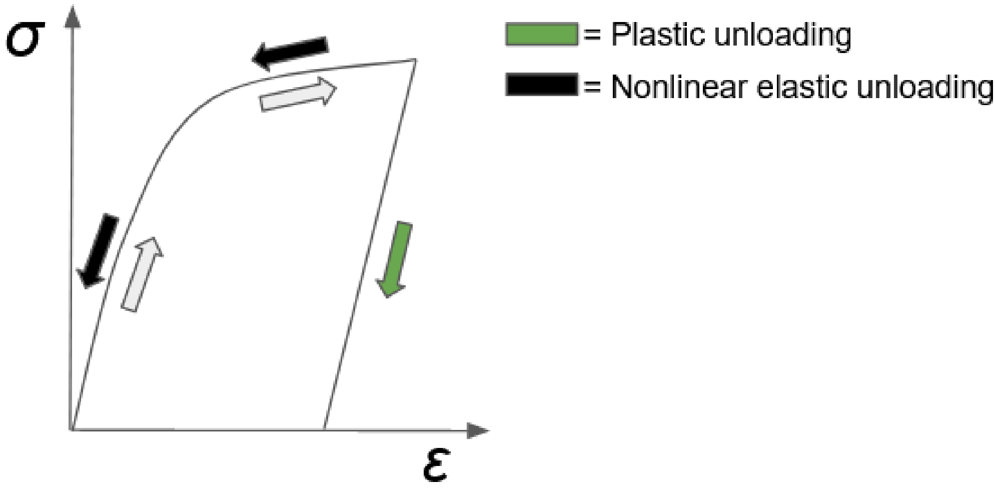


Figure 2.2: Nonlinear elastic behaviour vs plastic behaviour of metals [20]

around the crack tip. This method has been independently proposed by Cherepanov [12] and Rice [46], after which this method has been further developed by Hutchinson [25] and Rice and Rosgengren [47] in which it is assumed that the elastic plastic stress strain curve can be approximated by a nonlinear elastic curve. The reason for this assumption lies in the fact that if unloading occurs, the J-integral is no longer accurate, due to plasticity being irreversible. This assumption is also called the 'deformation theory of plasticity' [26].

This means that if the stresses in the material increase monotonically, the behaviour of both the nonlinear elastic and elastic plastic material is the same. Thus, the standard theory of plasticity is applicable to an elastic plastic material. The energy release rate J can then be written as a path independent integral [25] [47]. This means the J-integral can also be used to measure the stress intensity, and not just as a measure of the energy release rate [25] [47].

However, there are a few limitations to the J-contour integral, which become more obvious when the J-integral itself is explained. Imagine a two-dimensional plane around a crack tip, around which there is a path. This path can take an arbitrary shape, as long as it's either only counterclockwise or clockwise. In this two-dimensional space, the displacement of the crack tip as a function of the traction as well as the strain energy density influence the total energy confined in the path. The combination of these is taken as an integral and is the total energy confined within the contour. The resulting equation is :

$$J = -\frac{\mathrm{d}U}{\mathrm{d}a} = \int_{\Gamma} (W \mathrm{d}x_2 - T_{\mathrm{i}} \frac{\partial u_{\mathrm{i}}}{\partial \mathrm{x}_1} \mathrm{d}s, \tag{2.17}$$

where the change in energy $U$ over the change in crack length $a$ is represented by the integral of the work $W$ times the change in distance minus the traction on the contour times the change in displacement times the change in length of the in the contour. The stresses and strains used in the above equation are two-dimensional, which implies that the material is in plane stress or plane strain, i.e. the material has no variation is stresses or strains are zero in the direction perpendicular to the plane used for the two dimensional assumption, respectively. However, the three-dimensional model that can capture the third principal stress is no longer path independent and is thus no longer useful as a measure of the stress intensity [5] [1]. This means that the J-integral will be an inaccurate measure of the energy release rate in front of a crack tip with high triaxiality. However, the method used by Bass et al.[66] and also by Link et al.[31] makes use of the J-integral as a measure of the stress intensity. This is one part where the background information is lacking, with only a little research done [5]. Fortunately, it is possible to research the effect of constraint with this definition of the J-integral, since this research will be self-consistent with the research done by Bass [66] and Link [31].

## 2.3. The effect of constraint

As discussed earlier, it is important to have a good understanding of the effect of crack tip constraint on the cleavage fracture to find if a new failure criterion is viable, because the crack tip constraint directly influences the stress state in front of the crack tip. Constraint has an effect on the plastic deformation that guides the stresses around the crack tip, and thus also on the triaxiality [41] [55]. The triaxiality is defined as shown in equation 2.18 and is the hydrostatic stress in an element divided by the equivalent von Mises stress. Since this definition takes the full stress state of the element into account, the triaxiality can be used as a measure of constraint:

$$\frac{\sigma_{hydro}}{\sigma_{eq,mises}} = \frac{\frac{1}{3}(\sigma_1 + \sigma_2 + \sigma_3)}{\frac{1}{\sqrt{2}}\sqrt{(\sigma_1 - \sigma_2)^2 + (\sigma_2 - \sigma_3)^2 + (\sigma_3 - \sigma_1)^2}}, \tag{2.18}$$

in which $\sigma_1$, $\sigma_2$ and $\sigma_3$ are the maximum, middle and minimum principal stress respectively. Another approach to define constraint is to look at the difference between elastic and plastic strains. If the area around the crack tip has experienced yielding, there will be both elastic and plastic strain. The amount of plastic deformation depends on the hardening of the material and the geometry. In general, the elastoplastic crack tip stress and strain fields can then be determined using the relation as described by the work of Hutchinson [25] and Rice and Rosengren [47], which is also called the HRR field. This field can then be used to determine the $K_I c$ or $J_c$. The difference between the found stress intensity and the stress intensity predicted by the HRR field can then be used as a measure of constraint. However, it is suggested that the simple power law used in the determination of plastic material response is insufficient [37] [67].

These methods resolve around the difference between the actual stresses in the material and the HRR field, with the difference in results occurring due to differences in constraint. An example of this is the work done by O'Dowd and Shih [52] [53], which led to the development of the J-Q two-parameter model.

Further research on the effect of constraint by Ma [36], indicates that the local cleavage fracture stress depends on the geometry and the stress triaxiality. It was observed that the increase of the cleavage fracture stress with the level of triaxiality is less than that of the local yield stress. As a result, there is an inverse correlation between the local cleavage fracture stress and the macroscopic fracture toughness.

Testa et al. [55] also investigated the effect of constraint on cleavage fracture. In this paper, a micromechanical model is used to determine the stress states that need to occur for a particle to initiate fracture. This micromechanical model considers a unit-cell model, which relates macroscopic conditions to the stress state around the hard particles at the grain boundaries in ferritic steel. This unit cell model is used to determine critical fracture stresses under different levels of triaxiality. It is assumed that if this critical stress is reached, the resulting crack spreads far enough into the metal matrix to drive further growth. Using the results from numerical simulations such as the ones in this thesis, but with a different type of specimen, it was found that the stress state in the particle is very dependent on plastic deformation, as expected. This stress rapidly increases with plastic deformation until fracture occurs, and increases with growth of triaxiality. Since there is more plastic deformation in conditions of higher triaxiality, there is an inverse relation between the stress state and triaxiality, similar to the work of Ma [36]. The results of the numerical simulation indicate that triaxiality strongly affects the critical stress for fracture. Furthermore, the critical stress also depends on the geometry of the specimen, the temperature and the strain rate. The plastic constraint factor is defined as the ratio between critical stress and the yield stress. This plastic constraint factor was used to find the master curve, which agrees well with the experimental results. This means that triaxiality is expected to influence the failure criterion and thus must be taken into account when developing other failure criteria.

## 2.4. Flaws of the Beremin model

As mentioned in the previous sections, the Beremin model is a local approach method [9]. It does not evaluate fracture in terms of global parameters, as is done in conventional theories in fracture mechanics, such as the J-integral and the stress intensity factor. These theories suggest that when the crack driving force becomes larger than the fracture toughness, fracture will occur. However, in the local approach method, the assumption is made that any volume element can fracture, as long as a certain stress/strain state is reached. This means that the behaviour of many local small volume elements can be used to determine macroscopic fracture. From this point of view, the Beremin model is very useful, as it only uses the stresses in the plastic zone for its fracture criterion.

However, the calibration of the Weibull parameters used in the Beremin model has shown a tendency for the Beremin model to overestimate the $m$ and $\sigma_u$ [43]. It is suggested that $m$ and $\sigma_u$ are strongly dependent on the stress triaxiality. Despite these flaws, the Beremin model is still useful for this thesis project, as it is not the aim of the project to find an accurate value for the fracture toughness or show that the Weibull parameters are within certain bounds, but to find the effect of biaxiality on the stress state that causes fracture that is self-consistent with the result as seen in the papers of Bass et al. and link [66][27]. This means the Beremin model will be used to determine the cumulative failure probability curve.

## 2.5. Calibration methods

To determine the Weibull parameters $m$ and $\sigma_u$, a calibration method has to be chosen. The choice for a calibration method is important since this thesis looks for the effect of biaxiality on the failure distribution of steel and choosing a poor calibration method or a poor failure criterion might lead to inaccurate results. In the next part, the calibration method used for this thesis is discussed. It is also elaborated on why this calibration method is chosen.

There are many methods for calibration, with the most well known being the methods introduced by Minami, Brückner, Munz and Trolldenier [42] and Gao, ruggieri and Dodds[19].

In Minami's paper [42], a number of cleavage fracture experiments is run. For each of these experiments, the $J$-integral and the size of the plastic zone at each applied level of load is determined. The $J$-integral and plastic volume are then used to determine the Weibull parameters. This procedure was then applied to three CT specimens that varied in thickness and confirmed that the probability density is independent of the specimen size and the geometry of the crack. This means that the Weibull parameters $m$ and $\sigma_u$ are material constants.

However, in the work of Gao [19], it is observed that there is a strong dependency of the Weibull parameters on the number of critical $J$ values available when Minami's method is considered, with many tens of critical $J$ values being required to reliably measure the Weibull slope parameter. Only between 6 and 10 critical $J$ values are required to determine the median of the critical $J$ value. This means that the calibration method as developed by Minami [42] is very expensive in terms of time and resources.

Ruggieri et al. [50] made an effort to increase the reliability of the calibration method of Minami, and thus require less experimental results. They did so by assuming a fixed value for the Weibull slope parameter. However, it is observed by Gao et al. [19] that if the parameter $\alpha$ is removed as a variable, the calibration method leads to nonunique values of $m$ and $\sigma_u$.

In the work by Gao, Ruggieri and Dodds [19], a solution to the nonuniqueness problem is found by finding a relationship between constraint at the crack tip and the parameter $m$ by performing two sets of experiments, one in large scale yielding conditions and one in small scale yielding conditions. It is stated by Gao et al.[19] that two experiment sets with two different loading modes can used to calibrate $m$ as well. This is because the required difference between the experiment sets is that there is a different constraint in front of the crack tip. The full calibration method is then summarized as follows:

- Two sets of specimens, each having a different crack, are tested under ductile to brittle transition temperatures. The crack configuration must be chosen so that different levels of constraint are present for each crack. These sets produce two fracture toughness distributions.

- A three-dimensional finite element analysis of both crack configurations is performed. This analysis must be detailed enough to insure the Weibull stress vs the energy release rate is converged for the expected values of $m$ and the applied loading.

- If the stresses in an element are determined to be larger than the yield stress, the element is deforming plastically.

- If the element is deforming plastically, the stress acting in the element as well as the volume of that element are stored for each load step.

- For an assumed $m$, the Weibull stress is calculated for each loadstep in the finite element model and the result of the $J$-integral is stored.
- The measured toughness value of the set that experienced large scale yielding is corrected for constraint by using a toughness scaling model; $J_c \rightarrow J_{c,ssy}$. This means the toughness has been corrected as if the specimen fractured under small scale yielding conditions.
- The toughness values that are corrected for constraint are then used to determine the maximum likelihood value, called $\beta$, of each set:
$$\beta = [\frac{1}{r}(\sum_{i=1}^{r} J^2_{(i)-SSY})]^{1/2} \tag{2.19}$$
- Both values of $\beta$ are then used to construct the error function of the constraint correction. This is defined as $R(m) = (\beta_B - \beta_A)/\beta_A$. This value should be plotted for the expected range of $m$, and for the calibrated Weibull modulus, the error function should be 0, within a small tolerance.
- Once the Weibull modulus is calibrated, the $\sigma_u$ has to be found. The value of $\sigma_u$ corresponds to the value of $\beta_A = \beta_B = J$

This means that different specimens with different geometries can be used, as long as the temperature of testing is known and a relation between the J and the Weibull stress can be established. An example of an experimental setup that will satisfy this criterion is shown in appendix A.1.

However, it should be noted biaxial loading invalidates the plane strain assumption which is used to determine the $J$-integral as described by Rice [46]. In Rice's work, the $J$-integral is determined using the strains in the plane in the direction of the crack tip. Since the $J$ integral is found using FEM, for a three dimensional crack loaded biaxially, values found for the $J$-integral might not be accurate since the strains that are out of plane are not considered as part of the energy release rate. A three-dimensional $J$-integral would solve this issue, like the process used by Bakker [5], but is no longer path independent. As demonstrated by Rice [46], path indepency is required for the J-integral to act as a measure of the fracture toughness.

Despite the probable inaccuracy of the $J$-integral for biaxial loads, the results from both Bass et al. [66] and Link et al. [31] have been obtained with the two-dimensional interpretation of the $J$-integral. To ensure this thesis is self-consistent with the results as obtained by Link et al. [31] and Bass et al. [66], the two-dimensional interpretation of the $J$-integral will be used as well.

# 3

# Available Datasets

To determine the effect of the stress parameter on the Weibull distribution, a a suitable dataset is required. The datasets provided by Bass [66], The United States naval academy (USNA) [31] and the dataset from the European round robin [22] are all suitable for this thesis. Of these datasets, only the dataset by USNA has been used for this thesis, as it is the most complete dataset available.

## 3.1. Dataset United States Naval Academy

The dataset that is extensively used in this thesis is the one used by the US naval academy. Professors Link, Joyce and Roe found inconsistencies in the work of Bass et al. [31]. To investigate these inconsistencies, a new dataset was created using the Shoreham A533B plate as its basis. It is a pressure vessel steel that has been removed from the decommissioned Shoreham nuclear plant, after running on full power for only two days. The specimens were then cut from a section of steel that had been removed from a 150 mm thick shell plate. It was originally located just under the nozzle of the pressure vessel, which is located in the upper section of the vessel. This steel was then used to produce a variety of specimens.

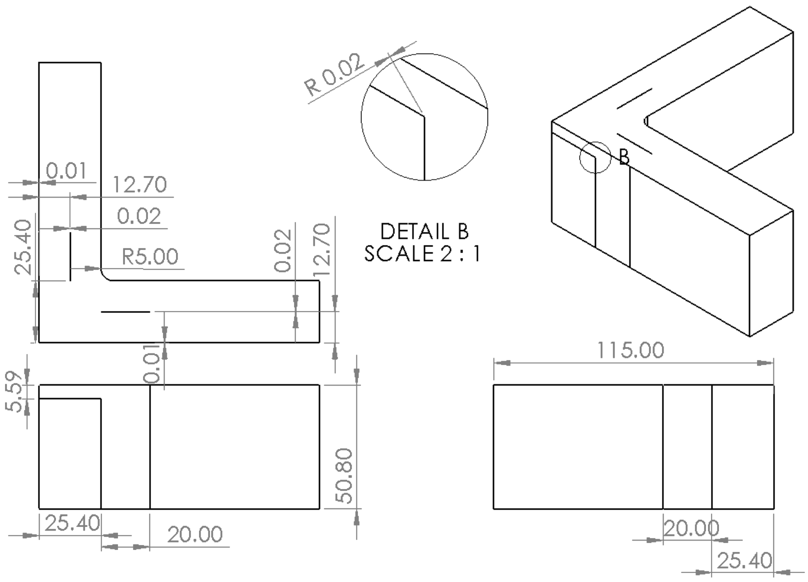


Figure 3.1: Dimensions in mm as used at USNA and as taken from [66]

## 3.2. Geometries used

The geometries used in the USNA dataset [31] are the cruciform specimen and SENB specimens with varying dimensions. In this thesis only the SENB specimens with a thickness of 1 inch are considered, also called the

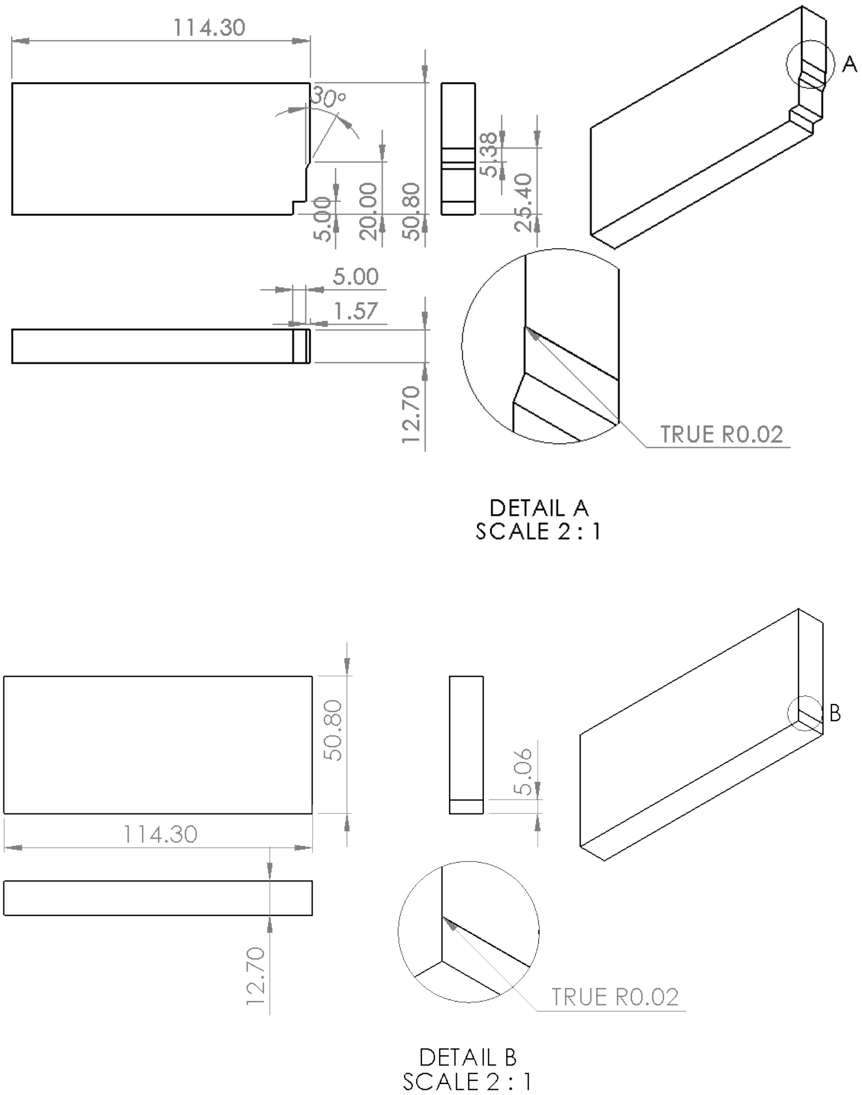


Figure 3.2: Deeply and shallow cracked specimens - Dimensions in mm as used at USNA and as taken from ASTM E1820 [3]

1T SE(B) specimen. For the rest of this thesis, whenever the SENB specimen is mentioned, this is the geometry referred to. The dimensions for the quarter symmetric cruciform specimens are shown in Figure 3.1. The dimensions for the quarter symmetric SENB specimens are shown in the Figures of 3.2. The two figures displayed are of the deeply and shallow cracked specimens respectively, as required by Gao's calibration method [19].

It is very important to note that the exact prefatigue regimen is not known for the cruciform and shallow SENB specimens. It is mentioned by Link et al. [31] that the stress intensity factor used during precracking is established using a three-dimensional finite element analysis of the cruciform geometry. It is not mentioned, but it is likely the same is done for the shallow and deeply cracked SENB specimens. However, the pre-crack for the deeply cracked specimen is known, being approximately 5.4 mm for an a/W of 0.5.

For this thesis the cruciform specimens tested at -100 °C are considered, since in the dataset results for both the biaxially and uniaxially loaded cruciform specimen are provided at -100 °C. Thus, also the results for SENB specimens at -100 °C are required. These specimens are placed in a supporting structure with a span of 400 mm between the rollers as shown in Figure 3.3. This structure is used to apply a certain biaxiality ratio on the specimen. A similar structure, also shown in 3.3, but with a span of 200 mm and with arms in only one direction is used for the SENB specimens, as derived from the standard by ASTM as described for SENB specimens [3]. In Link's work [31], the biaxiality ratio applied on the specimen is 1.2 to 1, which means that the load applied on the arm parallel to the crack is 1.2 times as large as the load applied on the arm perpendicular to the crack. While it is not specified in the paper by Link [31], creating this ratio was likely done by changing the distance of the arm.

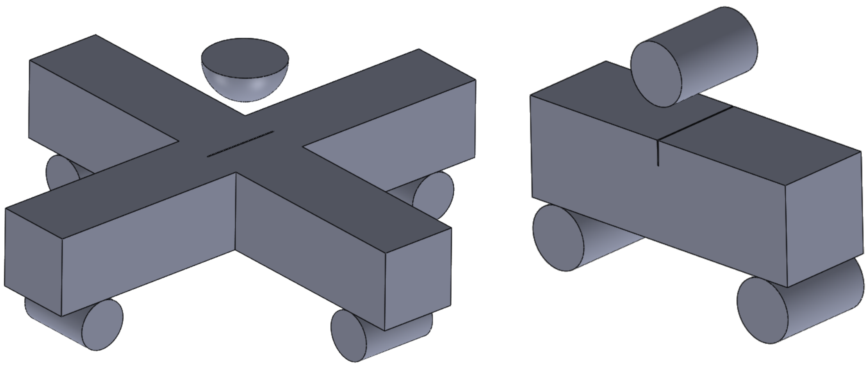

Figure 3.3: Supporting structures USNA for the cruciform and SENB specimen respectively, as specified in [31]

It should be noted that no suitable results for the SENB specimens were made available by Link et al. [31]. However, in Figure 3.4, the critical values for K have been reported for a temperature of -120 °C . Additionally, the master curve along with its 95% confidence bounds has been reported. However, since the slope of the master curve changes with respect to the critical fracture toughness of the specimen, it was not possible to directly use the master curve to determine the distribution at -100 °C . By analyzing the picture extensively, the critical K values have been determined with a $\pm 0.75$ MPa$\sqrt{\text{m}}$ accuracy. Then, a relationship was established between the critical K values at -120 °C with the expected critical K values at -100 °C. This was done using roughly the same process as the Gao calibration method. First the critical values at -120 °C were determined on the master curve and its confidence bounds. Then the same was done at -100 °C. To create a curve fit, the assumption is made that the relation between the critical values of K varies linearly. This means that essentially, for each specimen, a separate master curve was determined.

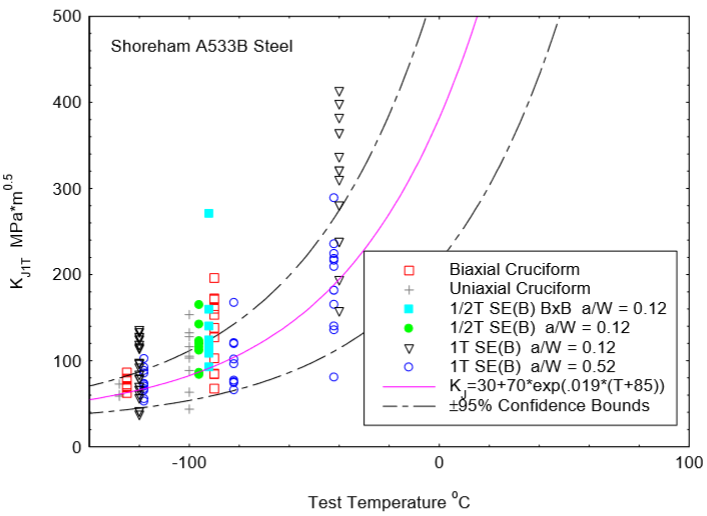


Figure 3.4: Critical K values versus the test temperature [31].

The results for the SENB specimen can be found in Appen Tables 3.1 and 3.2. These results are the ones that are used to calibrate the Weibull modulus using Gao's method. The results for the cruciform specimens are similarly described in Tables 3.3 and 3.4, with a distinction between the biaxially and uniaxially loaded specimens. In this dataset, it was shown that there was no biaxial effect on the master curve parameter $T_0$.

In short, it was found that the biaxially loaded specimens with shallow cracks show excellent agreement with the measured $T_0$ from the tested SENB specimens. It should be noted, that it was found that the $T_0$ measured by SENB specimens is dependent on which specimen is used, as a different type of specimens called the CT specimens produced different values for $T_0$ than SENB specimens. Thus the reference temperature for the master curve can be considered dependent on geometry.

This dependency on geometry makes it interesting to determine if the biaxial effect as observed by Bass et al. [66] still remains present in this dataset [31], When the Weibull distribution is used as a measure of the fracture toughness instead of the master curve.

$$\begin{aligned} \text{K at - 120 °C} &= 21.250x + 24.583 \quad \text{and} \\ \text{K at - 100 °C} &= 29.375x + 27.917, \end{aligned} \tag{3.1}$$

where x is a measure of how large the stress intensity is. The parameter x is determined using the reported values of the critical stress intensity from Figure 3.4, which is then used to determine the critical values of K at -100 °C. This means an additional error is added to the data, with the maximum error being around ±1 MPa$\sqrt{\text{m}}$. This means this procedure adds a maximum error to the data of approximately ±1.75 MPa$\sqrt{\text{m}}$, which was considered acceptable. The effect of this error is discussed in Chapter 5.

Table 3.1: Shallow cracked SENB specimens - Shoreham A533B plate[31]

| $K_{jc}$ @ -120 °C [MPa$\sqrt{\text{m}}$] | $K_{jc}$ @ -100 °C [MPa$\sqrt{\text{m}}$] | a/W [-] | $CMOD_c$ [mm] |
|---|---|---|---|
| 38.67 | 46.67 | 0.12 | 0.21 |
| 40.87 | 49.71 | 0.12 | 0.23 |
| 57.27 | 72.38 | 0.12 | 0.083 |
| 59.57 | 75.56 | 0.12 | 0.22 |
| 66.67 | 85.37 | 0.12 | 0.084 |
| 70.42 | 90.55 | 0.12 | 0.14 |
| 79.17 | 102.65 | 0.12 | 0.064 |
| 84.17 | 109.56 | 0.12 | 0.14 |
| 94.17 | 123.39 | 0.12 | 0.13 |
| 96.67 | 126.84 | 0.12 | 0.22 |
| 97.92 | 128.57 | 0.12 | 0.30 |
| 115.42 | 152.76 | 0.12 | 0.14 |
| 115.42 | 152.76 | 0.12 | 0.14 |
| 119.17 | 157.94 | 0.12 | 0.14 |
| 124.17 | 164.87 | 0.12 | 0.14 |
| 126.67 | 168.31 | 0.12 | 0.14 |
| 127.92 | 170.04 | 0.12 | 0.14 |
| 129.17 | 171.77 | 0.12 | 0.14 |
| 130.42 | 173.49 | 0.12 | 0.14 |
| 134.17 | 178.68 | 0.12 | 0.14 |
| 145.42 | 194.23 | 0.12 | 0.14 |
| 146.67 | 195.96 | 0.12 | 0.14 |
| 147.92 | 197.69 | 0.12 | 0.14 |

Table 3.2: Deeply cracked SENB specimens - Shoreham A533B plate[31]

| $K_{jc}$ @ -120 °C [MPa$\sqrt{\text{m}}$] | $K_{jc}$ @ -100 °C [MPa$\sqrt{\text{m}}$] | a/W [-] | $CMOD_c$ [mm] |
|---|---|---|---|
| 56.67 | 71.55 | 0.52 | 0.21 |
| 59.17 | 75.00 | 0.52 | 0.23 |
| 68.17 | 87.45 | 0.52 | 0.083 |
| 70.42 | 90.56 | 0.52 | 0.22 |
| 74.17 | 95.74 | 0.52 | 0.084 |
| 76.67 | 99.19 | 0.52 | 0.14 |
| 77.92 | 100.92 | 0.52 | 0.064 |
| 89.17 | 116.47 | 0.52 | 0.14 |
| 91.67 | 119.93 | 0.52 | 0.13 |
| 96.67 | 126.84 | 0.52 | 0.22 |
| 105.42 | 138.94 | 0.52 | 0.30 |

Table 3.3: Biaxially loaded cruciform specimens - Shoreham A533B plate[31]

| Specimen | Temperature [°C] | $K_{jc}$ [MPa$\sqrt{m}$] | a/W [-] | $CMOD_c$ [mm] |
|---|---|---|---|---|
| I4 | -100 | 145 | 0.119 | 0.22 |
| I5 | -100 | 106 | 0.104 | 0.14 |
| I14 | -100 | 122 | 0.112 | 0.17 |
| I3 | -100 | 128 | 0.108 | 0.18 |
| I12 | -100 | 79 | 0.109 | 0.090 |
| I1 | -100 | 157 | 0.114 | 0.26 |
| I13 | -100 | 113 | 0.109 | 0.15 |
| I11 | -100 | 123 | 0.103 | 0.17 |
| I6 | -100 | 50 | 0.111 | 0.053 |
| I8 | -100 | 67 | 0.109 | 0.074 |
| I7 | -100 | 94 | 0.109 | 0.10 |
| I2 | -100 | 108 | 0.115 | 0.14 |

Table 3.4: Uniaxially loaded cruciform specimens - Shoreham A533B plate [31]

| Specimen | Temperature [°C] | $K_{jc}$ [MPa$\sqrt{m}$] | a/W [-] | $CMOD_c$ [mm] |
|---|---|---|---|---|
| BXLS7C | -100 | 57.6 | 0.112 | 0.062 |
| BXLS8C | -100 | 79.6 | 0.121 | 0.09 |
| BXLS9 | -100 | 113.7 | 0.121 | 0.147 |
| BXLS10 | -100 | 103.6 | 0.122 | 0.147 |
| BXLS10C | -100 | 117.7 | 0.121 | 0.156 |
| BXLS11 | -100 | 40.6 | 0.132 | 0.043 |
| BXLS11C | -100 | 135.9 | 0.128 | 0.204 |
| BXLS12 | -100 | 102.9 | 0.125 | 0.108 |
| BXLS12C | -100 | 105.2 | 0.122 | 0.112 |

# 4

# Model used in simulation

To find the Weibull stresses from the data provided by the dataset of USNA [31], an Abaqus model is created, from which the stresses and strains during loading are derived. In order to do so, a material model is constructed, a mesh is created, the boundary conditions are identified and the finite element model is verified using the using the ASTM E1820 Standard [3] to compare results from the available dataset with results from a finite element experiment.

## 4.1. Meshing SENB specimen

The SENB specimen was modelled according to the Figures in section 3.2. Since the geometry of this specimen allows for a consistent type of mesh element, it is decided to use a hexahedral-dominated mesh over the entire specimen.

The smallest reported values of the crack tip opening displacement for the Shoreham pressure vessel steel has been approximately 0.04 mm, for a cruciform specimen. In general, the reported crack tip opening displacement are significantly larger, with the average crack tip opening displacement being around 0.12 mm. As reported in the work of Ruggieri [51] and Mcmeeking [40], the stresses around the crack tip become independent of the initial root radius if the crack tip opening displacement is larger than 4 times the root radius. This would lead to a crack tip radius of 0.01 mm However, the initial SENB and cruciform model were designed from the work of Bass [66], where the smallest reported crack tip opening displacement was reported to be approximately 0.08 mm. This means that a crack tip radius of 0.02 mm was chosen. The assumption was made that the relation of the root radius and the stresses does not change if either a SENB specimen is considered or a cruciform specimen. To find if these assumptions have a significant effect, the reported CTOD will be compared to the CTOD derived from the finite element model at the end of this chapter. The elements around the crack tip are meshed with 10 elements along its quarter-circumference, as can be seen in Figure 4.4. Radially, these lengths of these elements are changed to have small elements close to the crack tip, and larger elements further away from the crack tip. The smallest elements around the crack tip have a volume of around 7.5e-04 $mm^3$, with the average volume of the elements in the considered region being around 0.11 $mm^3$. Radially, the length of the elements close to the crack tip was around 0.02 mm. The approximate number of elements used in the SENB specimens is 10000. These elements are of the C3D8R element type, since it is a good general purpose element, and since it is linear, the amount of computational power required is also limited. It should be noted there is no real difference in the mesh around the crack tip for either the shallow or the deeply cracked SENB specimen.

## 4.2. Meshing Cruciform specimen

Similar to the SENB specimen, the Cruciform specimen is modelled according to the dimensions in Figure 3.1. The full cruciform test, loaded in only one direction, with its corresponding boundary conditions, can be seen in Figure 4.1. The locations where the meshing program of Abaqus presented difficulties are identified, as shown in Figure 4.2. The finished model can be seen in Figure 4.4.

The mesh itself is created with varying sizes over the full geometry. By only increasing the mesh density locally, such as the volume around the crack tip, the number of elements used is minimal. This is reasonable, as this thesis is focused on the stresses and strains around to crack tip, not on the rest of the specimen. Since the contact points of the model as described in Chapter 3 are far away from the crack tip, Saint-Venant's principle is applicable. Saint-Venant's principle states that if the loads are applied at sufficiently large distances, the effect of these loads becomes very small, as described by A. Love [32].

To model the crack tip, it is decided to use hexahedral elements, as hexahedral elements generally produce more accurate results than their tetrahedral counterparts [8]. Furthermore, hexahedral elements are more stable during numerical integration [8]. To allow for the mesh to transition to be more coarse in the arms, tetrahedral elements were used in the arms, as it is easier to mesh transitions and other strange geometries with tetrahedral elements rather than hexahedral elements.

To ensure a smooth transition from the tetrahedral dominated arms parallel to the crack to the structured hexahedral region around the crack tip, a hex-dominated region is placed between the crack tip and the cruciform arms. This ensures unexpected peaks in stresses that occur from the transition from tetrahedral to hexahedral elements do not influence the region around the crack tip. This transition is shown in Figure 4.3.

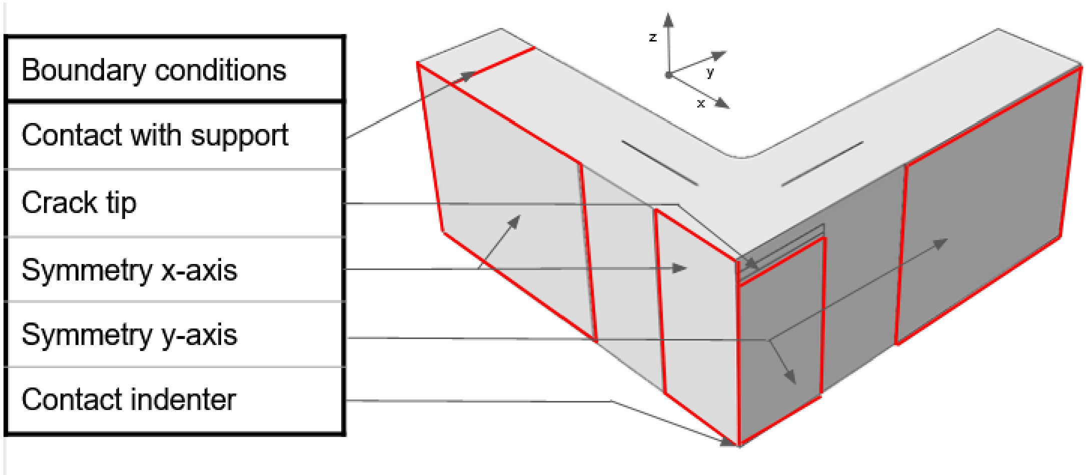


Figure 4.1: Uniaxially loaded model, with the boundary conditions included in the schematic

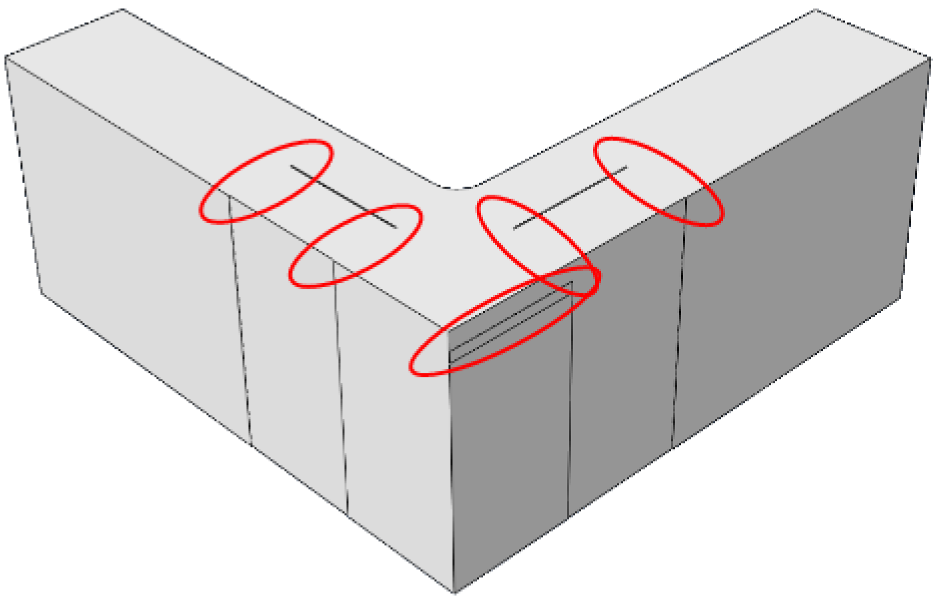

Figure 4.2: Locations where errors are likely to occur - cruciform specimen

Given that the reported values for the critical crack opening displacement as described are for a cruciform specimen, it was decided to keep the blunted 0.02 mm crack tip radius. Along this radius, 10 elements are placed, similar to the SENB specimen. To ensure the elements at the crack are small, a biased mesh is created that contains smaller elements close the crack tip and larger elements further from the crack tip. This is done

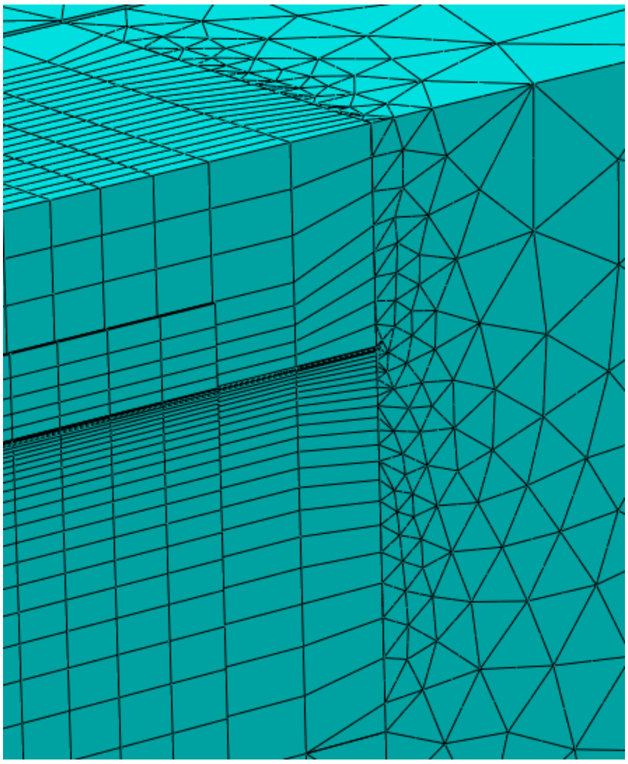

Figure 4.3: Transition from tetradral to hexahedral elements in the cruciform specimen.

to capture the extreme stress and strain gradients close to the crack tip. The smallest of these elements have a volume of around 10 $\mu m^3$, with the average volume of the elements close to the crack tip being around 0.1 $mm^3$. The radial length of the smallest elements are around 0.018 mm. The hexahedral element C3D8R is chosen for the elements around the crack tip, which is a good general purpose element [57]. C3D8R is a linear element type, which limits the amount of computational power required. It does have twelve zero energy nodes, which potentially leads to trouble with hourglassing. However, with hourglass controls being activated by default for this type of element, hourglassing is not significant in this model, except for large displacements. When the observed energy release rate is much higher than the critical energy release rates given by Link [31], some hourglassing does occur, but this does not influence the results as it occurs for higher energy release rates than the observed critical release rate.

The wedge elements are generated to ensure compatibility between hexahedral-dominated mesh elements; this is necessary due to the choice for the hexahedral-dominated mesh assigned to the area close to the crack tip. It should be noted that the wedge elements are at least 20 elements away from the crack tip. The tetrahedral elements were chosen to be quadratic to ensure a proper transition from the hexahedral-dominated region to the tetrahedral-dominated region without significant stress peaks. The transition between the tetrahedral and hexahedral dominated region is created by applying a tie constraint between the contact surfaces of the regions. This tie constraint ensures nodes along the surface experience the same movement, which means that forces and stresses experience a smooth transition between the tetrahedral and hexahedral regions.

The resulting mesh around the crack tip is shown in detail in Figure 4.4. The used elements in the finite element model can be summarized as follows and is approximately the same for each the specimens, even though the depth of the crack varies slightly:

- Total number of elements: 34000
- 18000 linear hexahedral elements: type C3D8R [Used around the crack tip]
- 2300 linear wedge elements of type C3D6
- 13700 quadratic tetrahedral elements of type C3D10

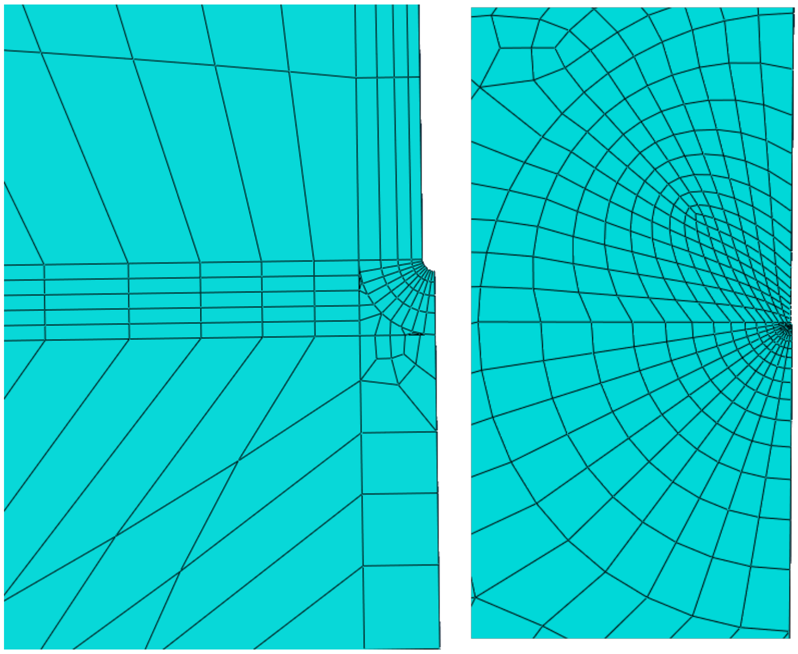

Figure 4.4: Mesh close to the crack tip for the cruciform and SENB specimen respectively. Crack tip radius is 0.02 mm - cruciform specimen, with the crack oriented towards the top of the page.

## 4.3. Convergence study

To ensure that the mesh produces accurate results for the J-integral, the stresses and the strains, a mesh convergence study is performed on the cruciform model. The goal of this mesh convergence study is to twofold; it ensures that the chosen size of the mesh lies in the convergence region, where the results of the finite element model no longer vary with mesh size. It also measures if the chosen mesh size is computationally efficient, i.e. the amount of time the simulation requires is minimal. This convergence study was performed by altering the mesh density in the area close to the crack tip, as shown in Figure 4.5. Afterwards, the stresses and the energy release rate around the crack tip are determined for 4 different mesh densities. It should be noted that the largest difference in mesh density is very close to the crack tip, as can be seen in Figure 4.4. Four different mesh sizes were chosen, which change the density of the mesh close to the crack tip, especially focusing on the aspect ratio of the elements and the density very close to the crack tip. These different meshes are conveniently called coarse, semi-coarse, semi-fine and fine, with semi-fine being the mesh used in the simulations. The difference in volume of the smallest element is representative of the change in mesh size and volume, with coarse having a smallest element volume of 1.5e$^{-4}$ mm$^3$, semi-coarse having 4.0e$^{-5}$ mm$^3$, semi-fine having 2.8e$^{-5}$ mm$^3$ and fine having 1.5e$^{-5}$ mm$^3$.

The different mesh sizes can be seen in Figure 4.6, with more detail being shown in Figure 4.7. It is observed that the results are already very similar. No difference in results is observed for the semi-coarse, semi-fine and fine meshes, while the difference with the coarse mesh is small, even with the significantly larger mesh volume. These results can be seen in Figure 4.8. Additionally, the energy release rates of the coarse and fine mesh are almost identical, as seen in Figure 4.9, and the results again become indiscernible from each other for the semi-coarse, semi-fine and fine meshes. This means mesh convergence has been achieved. Based on these results, it was decided to use the semi-fine mesh density for the finite element model.

## 4.4. Material properties

The material properties are determined using tensile stress/strain data provided by professor Link [30]. The Young's modulus is determined by identifying the yield strength and the critical strain for which this yield strength occurs. It has also been determined by fitting a line through the linear elastic portion, and this produced the same result. This is a good indication that the found young's modulus is reasonable.

After the yield strength of the material has been reached, the plastic material behavior is modelled using

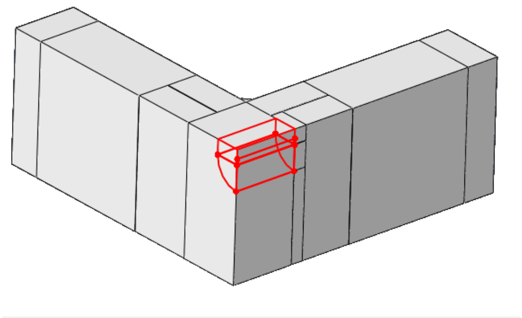

Figure 4.5: Volume where mesh density is altered for the mesh convergence study

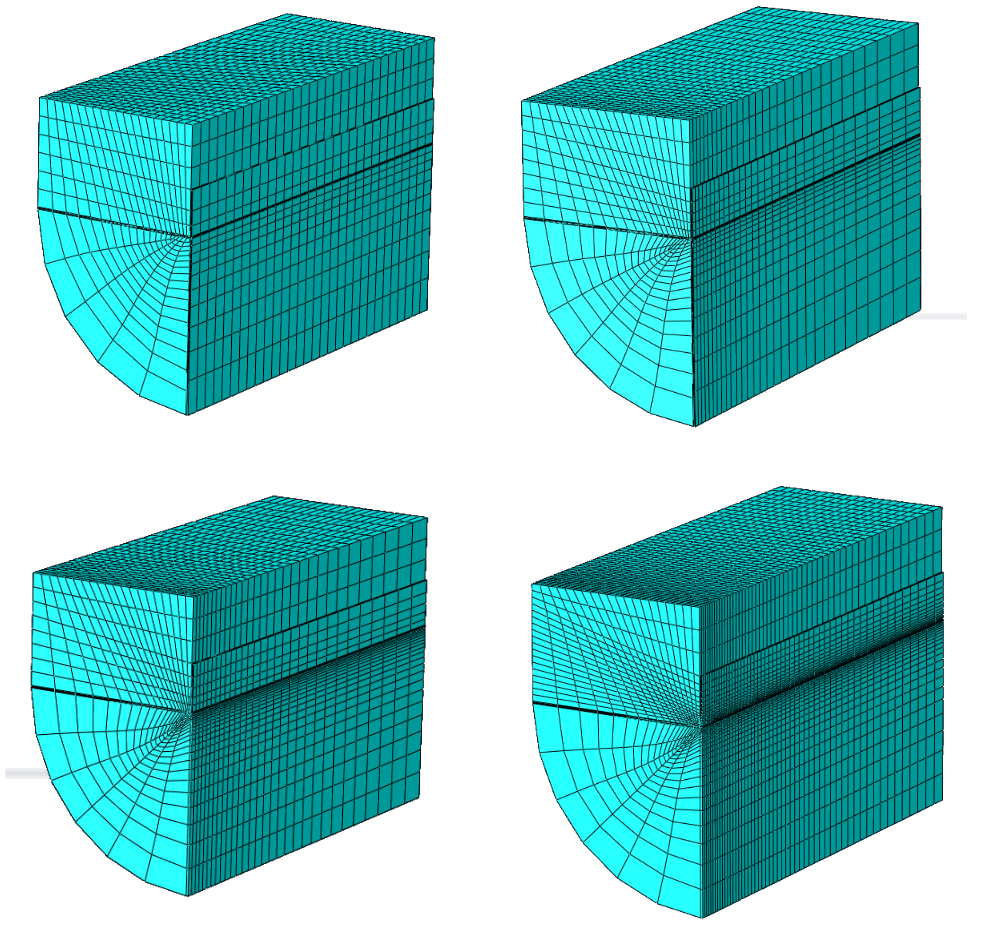

Figure 4.6: Varying mesh densities; coarse, semi-coarse, semi-fine and fine respectively

one of the power laws that can approximate strengthening of the material. The Voce, Hollomon and Swift power laws were used to determine the material response. These equations are known as follows:

- Voce:

$$\sigma = a - b - (a - b)e^{-c\cdot\epsilon} \tag{4.1}$$

- Hollomon:

$$\sigma = a\cdot\epsilon^{b} \tag{4.2}$$

- Swift:

$$\sigma = a\cdot(\epsilon + b)^{c} \tag{4.3}$$

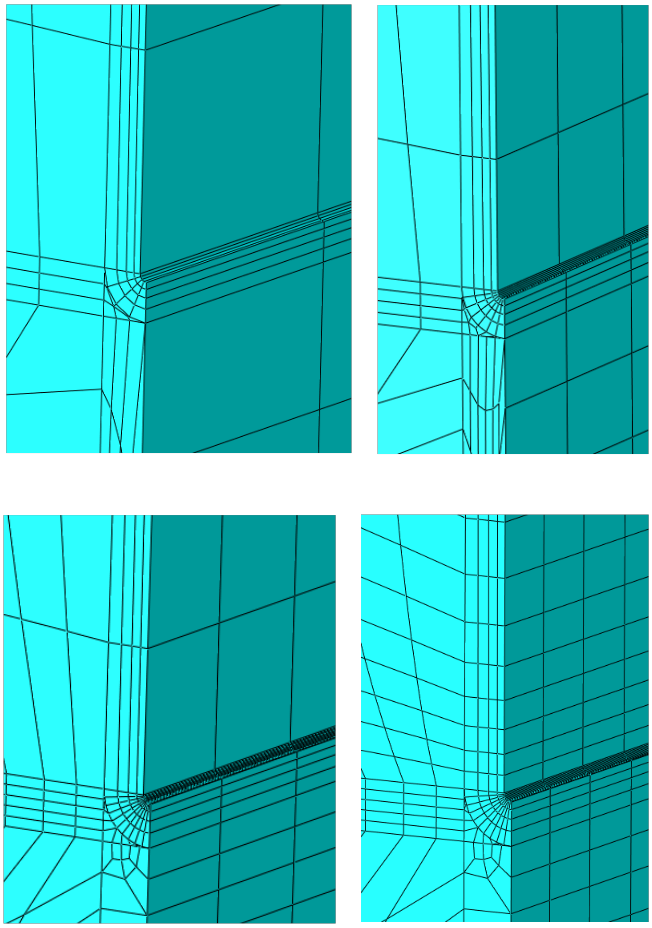

Figure 4.7: Detailed view of the crack tip; coarse, semi-coarse, semi-fine and fine respectively

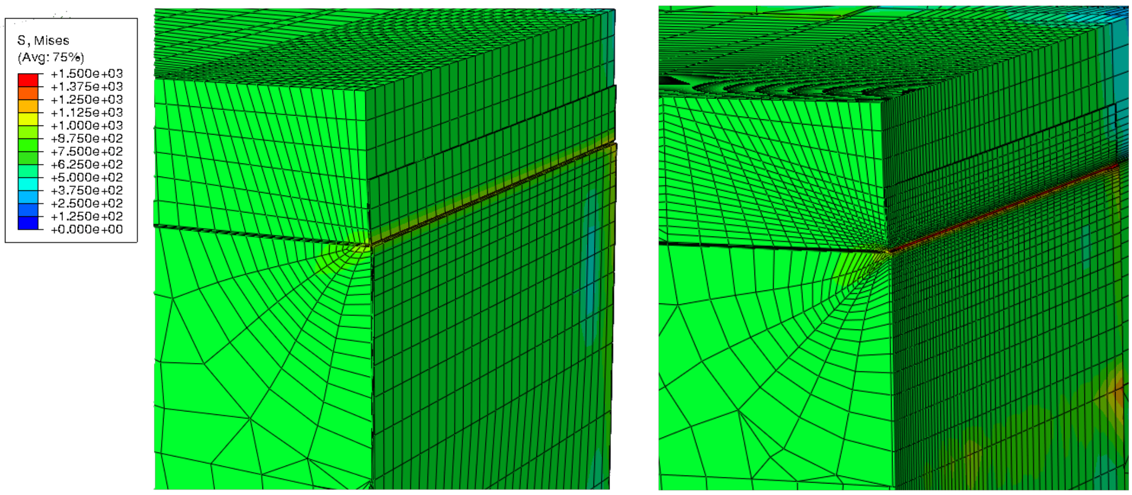


Figure 4.8: Stress in the coarse and fine mesh, respectively

The a, b and c parameters are then determined using a non-linear least squares function to fit the given function to the provided data by Link [30]. These material responses are then plotted with the experimental stress/strain data. It should be noted that the original stress/strain data only provided data until approximately 0.2 strain. In order to capture the high stresses and strains in front of the crack tip, the power laws

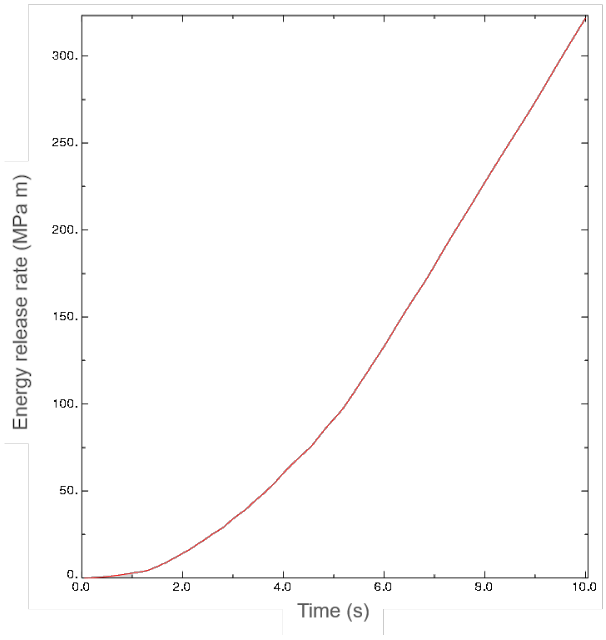


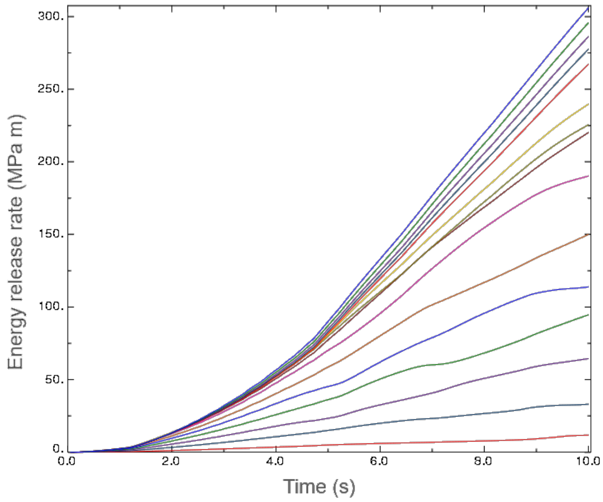


Figure 4.9: Energy release rate in the largest defined contour around the crack tip in the coarse (contour = 10) and the energy release rate over all contours of the fine mesh (contours = 1-15), respectively

were used to extrapolate the data up to 3.0 strain. This process was repeated for each temperature and specimen, with the average and best fitting power law being chosen to describe the material response. Since there was no stress/strain data for -100 °C, a linear interpolation was made between the stress/strain data of -80 °C and -120 °C . The power law that best described the material behaviour at -80 °C was Hollomon's law, while at -120 °C the Voce law described the material properties best.

Table 4.1 shows the Young's modulus and yield strength determined from this approach. Then the elastic plastic response for -100 and -120 °C is shown in Figures 4.10 and 4.11 respectively.

Table 4.1: Linear elastic data from stress/strain experiments Shoreham A533B steel, fitted using the data from Link [30]

| Temperature | Youngs Modulus [GPa] | Yield strength [MPa] | Poisson's ratio [-] |
|---|---|---|---|
| -100 °C | 225 | 670 | 0.3 |
| -120 °C | 231 | 685 | 0.3 |

Now that material models have been assumed, it is important to realize that the these models are only representations of reality, as all power laws are fitted to given data. The fit of the predicted plastic stress/strain curve shows good agreement with the observed plastic stress/strain curve for small strains. However, the small error at 0.14 strain in Figure 4.11, might translate into larger errors when significantly larger strains are considered, such as in this thesis. Hence, an estimation of this error at the largest possible strain was made by looking at the change in error between the physical stress/strain data and the predicted stress/strain data by the power law for the last few instances of provided experimental data. The average change in error was then assumed to be a constant and used to find the estimated error at 1.0 strain. This is best seen in Figure 4.12, where the stress/strain data has been plotted as well as the expected stress strain results. The estimated errors are shown in table 4.2 and indicate that there will be an error present in the plastic stress/strain prediction because of the extrapolation. However, since this error is assumed to be relatively small, it should not influence the final result of the FEM simulation significantly. Additionally, as long as the resulting error of the predicted plastic stress/strain curve remains consistent between the physical cruciform specimens and the model, the resulting data is still use able, since all data from the Abaqus model will return with the same error.

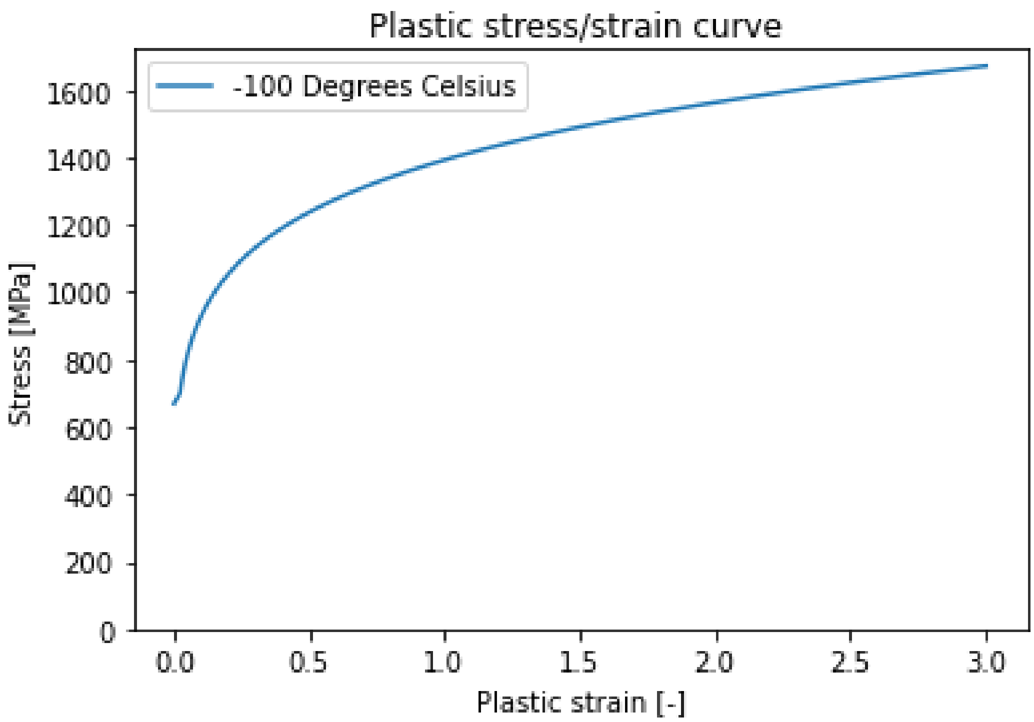


Figure 4.10: Elastic-plastic response for -100 °C Shoreham A533B steel

Table 4.2: Estimated error in power law

| Temperature [°C] | Estimated error [%] | Applied power law |
|---|---|---|
| -120 | 1.26 | Voce |
| -80 | 3.98 | Hollomon |

## 4.5. Boundary conditions

The six degrees of freedom of the finite element models have to be constrained to ensure the results will converge to a single stable result, as well as being as realistic as possible. Additionally, as mentioned in chapter 3, the models were all created as quarter symmetric models, where on the symmetry planes the corresponding symmetry is applied. This is shown in Figure 4.1. Additionally, the locations where the cruciform specimens rest on the supports are identified, and on these locations, boundary conditions are applied so that the biaxiality ratio as specified in the work of Link is satisfied [31]. The boundary conditions on the line where the support comes in contact with the specimen are as follows:

- Rotation around the axis perpendicular to the red line and the z-direction is set to 0. It should be noted that the red line is rotated 90 degrees for the biaxially loaded specimen.
- Translation in the y direction is set to 0. This is not realistic, as it will prevent contraction. However, the effect of the resulting stresses on the stresses around the crack tip is negligible. Because of this and the need to fully constrain the Cruciform and SENB specimens, it is decided to use this boundary condition. Furthermore, note that the direction of the translation changes when another arm of the cruciform model is constrained.
- Translation in the z-direction is set to -4 mm in the case of uniaxial loading and -4 and -4.8 mm in the case of biaxial loading, to simulate the 1:1.2 conditions around the crack tip. On the SENB specimen, this displacement is set to -4 mm.

All other degrees of freedom are not limited by this boundary condition, to allow the behaviour of the cruciform specimen to be realistic.

The final boundary condition, which is used to enforce the displacement of the cruciform model, is placed on an analytical rigid surface. This rigid surface is modelled as a hemisphere, and is used as the indenter, as

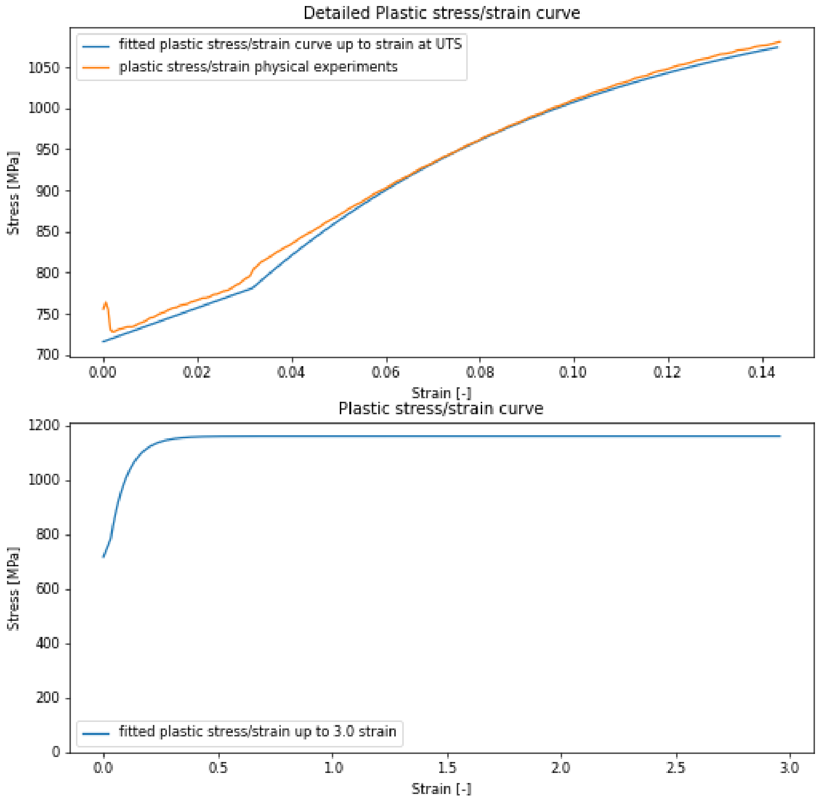


Figure 4.11: Estimated elastic-plastic response of Shoreham A533B steel at -120 °C, fitted using the data from Link [30]

shown in Figure 3.3. This indenter is constrained to have no displacement and rotation in all degrees of freedom. The same boundary conditions are applied on the indenter used in the SENB FEA model, but this indenter is cylindrical instead of spherical.

Finally, the contact surfaces are modelled using the general contact function in Abaqus, with a frictionless contact. Since the movement of the indenter is perpendicular to the surface of the cruciform specimen, the assumption that no friction occurs is a good approximation. Then the two surfaces that touch are identified, with the master surface being the analytical rigid body and the slave surface being the bottom face of the cruciform specimen. This means that in Abaqus, the stiffer surface is deforming the less stiff surface. Additionally the option to prevent overclosure is selected. This option ensures that the two surfaces are directly connected with very limited penetration happening. This prevents errors from occurring in the case of large penetration, as it prevents large penetration altogether.

## 4.6. Solution method and time steps applied

The solution technique used for this thesis is the full Newton method, which is generally used for nonlinear solutions, similar to the one in this thesis. While the full Newton method is computationally expensive, as the Jacobian has to be recalculated for each iteration, the size of the finite element model is not so large that another solution method is required. Additionally, the full Newton method is accurate since the time step is small. Finally, the precision of the solution was chosen to be single precision. The reasoning behind this decision was that accuracy of the result does not matter as much in this thesis, the effects of the biaxial loading is more important.

The FEA model itself is run using a static timestep of 0.05 seconds in the case of the cruciform model. For the SENB specimen, a timestep of 0.5 seconds is used. The simulation runs for 10 seconds, during which the

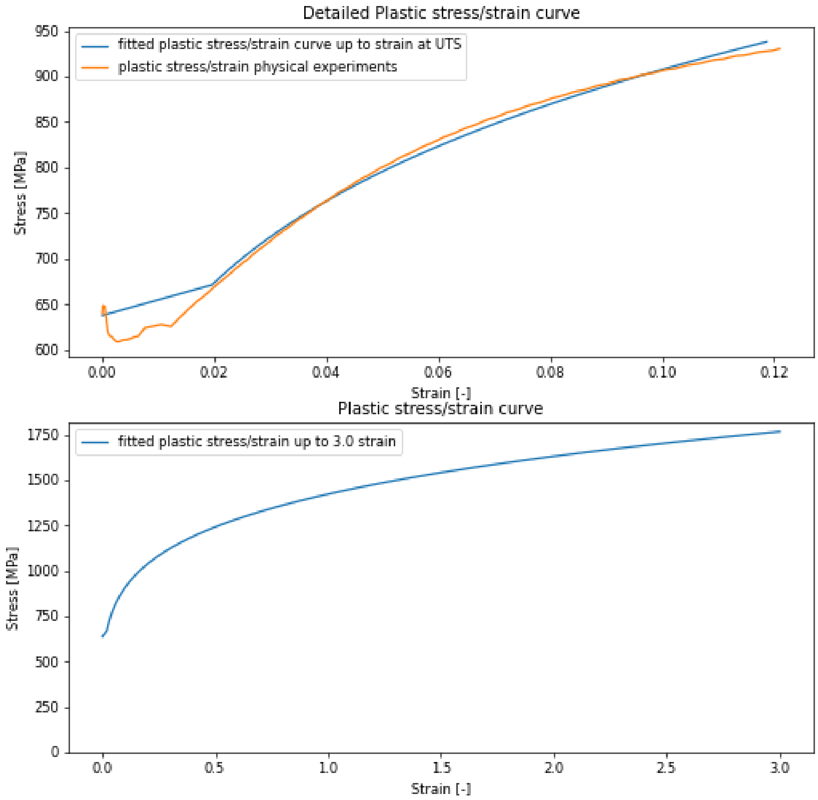


Figure 4.12: Estimated elastic-plastic response of Shoreham A533B steel at -80 °C, fitted using the data from Link [30]

displacement and load increase linearly until they reach their maximal values at 10 seconds.

Additionally, the effects of nonlinear geometry are included as well, as small changes in rotation can lead to drastically different results for the principal stress if local material directions are not rotated with the deformation in each element. Despite the displacements being relatively minor, on the order of a few mm, nonlinear geometry is still applied, which allows the internal coordinate system used for the material to model to rotate as well. This is because directions of the stresses and strains around the crack tip are very important to this thesis, and plasticity around the crack tip means that the material can no longer be considered fully isotropic.

## 4.7. Model verification

To confirm that the model can accurately predict the energy release rate, a SENB specimen with a thickness of one inch has been constructed in accordance to the ASTM E1820 standard [3]. Using this standard, it is possible to construct a relationship between the applied load, the force-displacement curve and the energy release rate. First the stress intensity factor K is determined, after which the elastic portion of the energy release rate $J$ is determined using the plane strain assumption, shown in equations 4.4 and 4.6. For this simulation, the material properties for structural steel are considered:

Table 4.3: Linear elastic data from stress/strain experiments structural steel [10]

| Youngs Modulus [GPa] | Yield strength [MPa] | Poisson's ratio [-] |
|---|---|---|
| 207 | 250 | 0.3 |

$$K = [\frac{PS}{(BB_n)^{\frac{1}{2}} W^{\frac{1}{2}}}] \cdot f(a/W), \tag{4.4}$$

with P being the applied load, S the distance between the supporting arms and always 4 times the width, B being the thickness of the SENB specimen and B always being half the width and finally W being the width of the SENB specimen, in this case being equal to 50.8 mm. The function f depends only on the crack depth compared to the width of the specimen.

$$J = \frac{K^2(1-\nu^2)}{E} + J_{pl} \tag{4.5}$$

with the plastic portion of the energy release rate being calculated as

$$J_{pl} = \frac{\eta_{pl} A_{pl}}{B_n b_0}, \tag{4.6}$$

and with $\nu$ being the Poissons ratio and E being the Youngs modulus. The plastic energy release rate depends on the area under the force/displacement curve, the value $\eta_{pl}$, the net specimen thickness $B_n$ and the notch depth $b_0$ [3]. It should be noted that the value of $\eta_{pl}$ depends on which method is used to determine $A_{pl}$. However, the experimental force/displacement curves are not available for the Shoreham material. This means that the plastic contribution of the J-integral can not be accurately determined. In order to still check if Abaqus produces results in line with the predictions from the standard [3], it was chosen to test with a small load, which is applied to the finite element model. In this case, a load of 2 kN has been used, which hopefully produces a mostly elastic result . This leads to a predicted energy release rate of approximately 0.061 kJ/$m^2$.

This is then compared to the result of the converged energy release rate for the FEM model, as seen in Figure 4.13. In this figure, each of the lines represents a contour used in Abaqus. These contours are located at the edges of elements close to the crack tip. This means the first contour, the one with the lowest energy release rate, has a contour of 1 element around the crack tip, while the second contour is located 2 elements away, and so on. It is seen that when the contour becomes larger, the predicted energy release rate converges, which is as expected when Rice's theorem is considered [46]. When the model has been loaded to 2 kN after 10 seconds, the converged value as found by abaqus, is found to be 0.07 kJ/$m^2$. This a significant difference with the predicted 0.061 kJ/$m^2$, but can easily be explained, since the plastic portion has not been taken into account in the predicted energy release rate. If the load at 4 seconds is taken into account, being 800 N, the predicted energy release rate becomes approximately 0.01 kJ/$m^2$, which is very close to the value of the energy release rate at 4 seconds in Figure 4.13. Since there will be little to no plasticity in the model at this point, the elastic part of equation 4.6 thus accurately predicts the energy release rate if there is little plastic deformation. Hence it is concluded that it is very likely that the total energy release rate $J$ as predicted by the FEM simulation is accurate, which takes both elastic and plastic energy release rate into account.

Table 4.4: Reported CTOD [30] vs CTOD from FEA

| Specimen | Reported CTOD [mm] | CTOD FEA [mm] |
|---|---|---|
| BXLS7C | 0.0625 | 0.0734 |
| BXLS8C | 0.0904 | 0.0952 |
| BXLS9 | 0.147 | 0.129 |
| BXLS10 | 0.147 | 0.134 |
| BXLS10C | 0.156 | 0.147 |
| BXLS11 | 0.043 | 0.069 |
| BXLS11C | 0.204 | 0.154 |
| BXLS12 | 0.108 | 0.100 |
| BXLS12C | 0.111 | 0.111 |

Finally, the observed crack tip opening displacement (CTOD) of the uniaxially loaded cruciform specimen, as reported in the data provided by link [30], is compared with the crack tip opening displacement as found by the finite element model. The results are shown in Table 4.4. As discussed previously, the smallest crack tip opening displacement is around 0.04 mm. It is observed that the finite element model produces a significantly larger value of the CTOD. These differences are not as large for the other specimens, with the

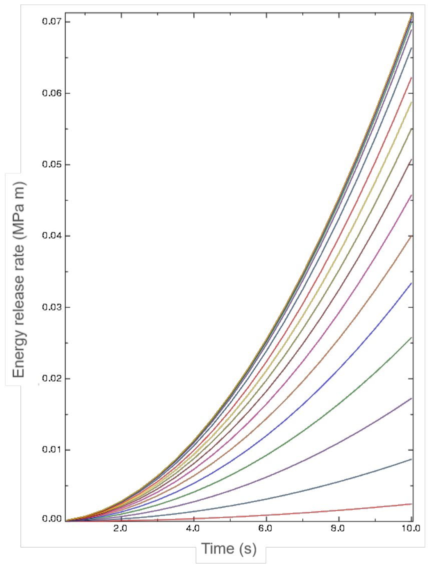


Figure 4.13: Energy release rate convergence and values between 0 and 2 kN for contours [1-15].

exception of the BXLS11C specimen, which experienced a significantly larger CTOD than found by the finite element model. While an error remains for almost all of the specimens, this could be due to discrepancies of the material model with the actual material, or due to the way the specimen is loaded. The results do indicate that the finite element is reasonably close to the tested specimens in the work of Link [31]. Hence, it is concluded that this model will produce reasonable results.

# 5

# Calibration method, Beremin model verification and tested failure criteria

In this chapter the calibration process is discussed, as originally proposed by Gao [19]. Additionally, further verification of the Beremin model is given. Finally, the applied failure criteria for this thesis are discussed.

## 5.1. Calibration procedure

After the finite element model has concluded its simulation, the stresses and strains around the crack tip, as well as the displacements, energy release rate $J$ and the triaxiality of the elements around the crack tip are determined. This data can then be used calibrate the Weibull parameters $m$ and $\sigma_u$. The calibration method used is derived from Gao's paper [19] and can be summarized as follows:

- For each frame of the simulation, the Weibull stress is determined for a Weibull modulus $m$ between 1 and 50.
- The J-integral is retrieved from the FEA output files, and it is plotted against the Weibull stress found in the prior step for all values of $m$ that were considered.
- Using the results from the prior step, a scaling relationship is determined, called the toughness scaling model. The critical $J_c$ values for the shallow and deeply cracked SENB specimens as reported in Link's paper[31] are then used to identify the loading for which the scaling model is applied. This is best understood as constructing a relationship between the constraint around a crack tip for a shallow cracked SENB specimen and the constraint around a deeply cracked SENB specimen. This allows for an estimation of the J-integral for shallow cracked specimens as if they were small scale yielding, as opposed to the large scale yielding that actually occurs. This is illustrated in Figure 5.1.
- The maximum likelihood of the new set of $J$ values can then be compared to the maximum likelihood of the set of critical $J$ values for the deeply cracked specimen. The Weibull modulus is successfully calibrated if for the $m$ that is found, the R(m) has become 0. The R(m) is simply the maximum likelihood of the deeply cracked specimen minus the maximum likelihood of the Weibull stress of the toughness scaled shallow cracked specimen.

## 5.2. Beremin model verification

Three parameter Weibull and two parameter Weibull distributions are possible, but it was found that three parameter Weibull distributions show better agreement with results [68][9][66]. In the three parameter Weibull distribution, the Weibull stress must have passed a critical value, which is assumed to be the Weibull stress when the stress intensity factor is large enough. In the case of ferritic steels, this stress intensity factor is 20 MPa$\sqrt{\text{m}}$, according to ASTM E-1921 [4] and also by Wallin for a 25 mm thick specimen [59]. This parameter is called the $K_{c,min}$. Wallin has extensively researched this parameter [60][59], and found that this parameter is temperature and thickness dependent, but calibrating this value requires a large number of specimens. Since

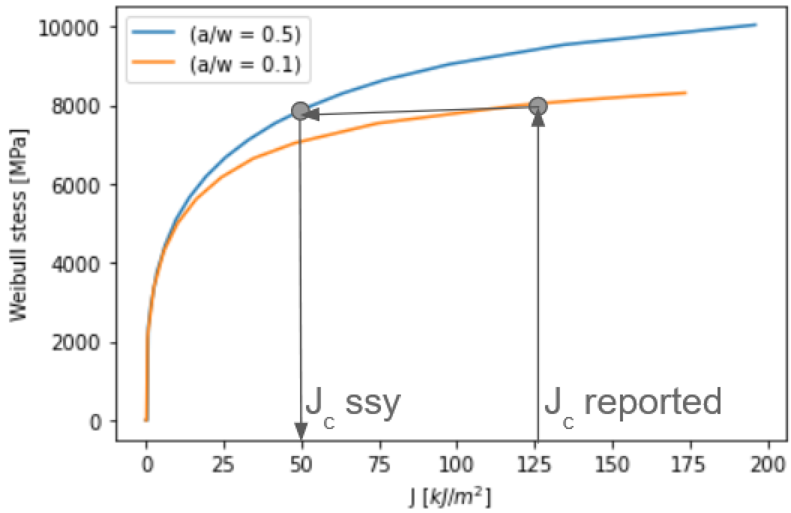


Figure 5.1: Toughness scaling model, showing the process from Large scale yielding to small scale yielding

choosing this value should already ensure the three parameter Weibull distribution shows better agreement than a two parameter distribution, it is assumed that a stress intensity factor of 20 MPa$\sqrt{\text{m}}$ is a reasonable estimate, as observed by Wallin [59]. To verify that the $K_{c,min}$ produces the best result possible, a variety of stress intensities have been plotted.

The difference between using a $K_{c,min}$ of 5, 10 and 20 MPa$\sqrt{\text{m}}$ is shown in Figure 5.2 along with the failure probability of the SENB specimens when calibrated using the hydrostatic stress criterion. From this figure, it is clear that the hydrostatic result fits the three parameter failure probability better when using the 20 MPa$\sqrt{\text{m}}$ stress intensity than the other two intensities. When larger values for $K_{c,min}$ are considered, the results start diverging , with the slope becoming steeper than the distribution of the SENB specimens. The found result of 20 MPa$\sqrt{\text{m}}$ approximately matches the value reported by Wallin [59] and is considered to be the conventional value for ferritic steels [19][1]. Thus a stress intensity of 20 MPa$\sqrt{\text{m}}$ will be used in the rest of the thesis.

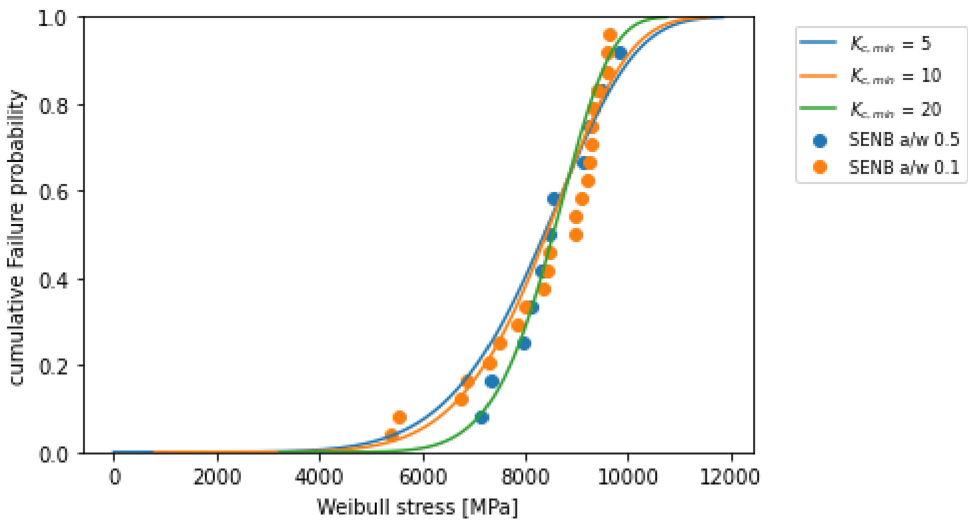


Figure 5.2: The Weibull distributions for $K_{c,min}$=5, 10 and 20 MPa$\sqrt{\text{m}}$.

## 5.3. Cumulative error

As mentioned in the previous chapters, it is possible to estimate the error in the determination of the critical fracture toughness values. The critical values of the stress intensity as derived from the USNA dataset have a maximum error of approximately 1.75 MPa$\sqrt{\text{m}}$. Additionally, the error due to the choice of material model can be estimated, with the stresses predicted by the model having an maximal error of approximately ± 3%. Thus, this error is also included in the impact determination of the cumulative error.

This means that the calibration procedure will have a confidence interval, which will be explored here. By calibrating the Weibull stress for the critical K values in which the estimated error is included and using the maximum principal stress as the failure criterion, the effect of the error can be investigated. The maximum principal stress criterion was chosen as it is the most common failure criterion that is used for fracture toughness determination, i.e. mode I. As can be seen in Figure 5.3, this error leads to a significant difference in the predicted Weibull stress and probability density function, as the calibration method produces small variations in the Weibull modulus $m$ for variations in the values of $K_{jc}$ used as the input for the calibration.

Another error that is important is the difference in predicted stresses by the material model. As shown in Chapter 4, the predicted stresses in the material can differ up to 3%. This effect is shown in Figure 5.4 and similarly to the error estimation by the $K_J c$, the error is significant.

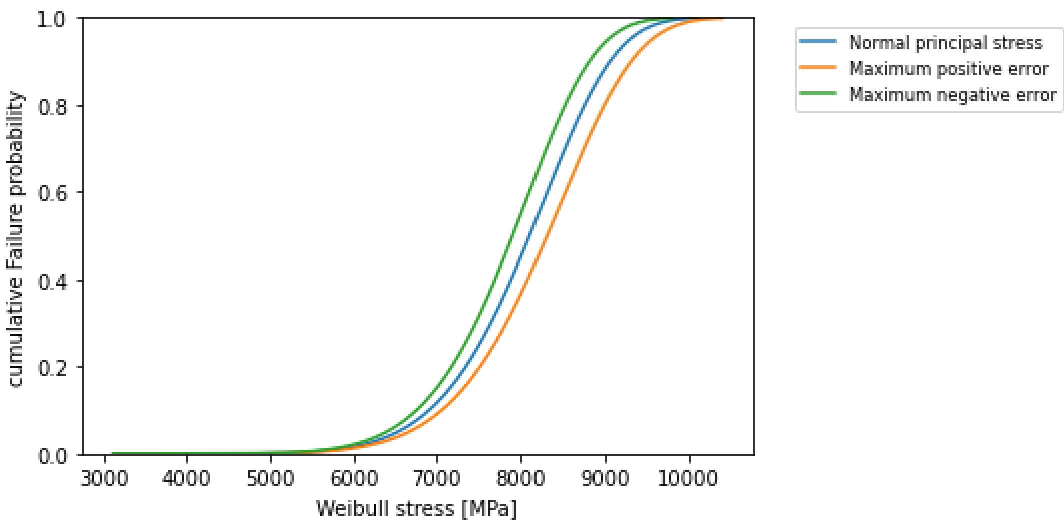


Figure 5.3: Estimation range error $K_{jc}$ values

However, while the presence of an error changes the results significantly, it does not change the effects of biaxial loads and the stress state on the Weibull stress. It does change the values obtained, but this error is taken into account with the calibration of the Weibull parameters. This means that the process as it is, is usable to determine the effect of multiaxial loading, but should not be used as is to find accurate values for the Weibull stresses.

## 5.4. Tested Weibull stresses

Other than the failure criteria mentioned in the paper by Bass [66], additional failure criteria are considered in this thesis, which may capture the underlying physical mechanisms behind biaxial fracture. As shown in Chapter 2, there are very few failure criteria found in the literature that deal with biaxial loading and different constraints. Only some of the Weibull stress criteria as considered by Bass et al. [66] are implemented in this thesis. This is because for the determination of the normal averaging, the coplanar energy release rate and the noncoplanar energy release rate, the exact orientation and location of the elements have to be known. To find this, additional data is required from the finite element model, as well as a very precise knowledge of the location of the integration point of the element. Since these failure criteria do not show an effect when a multiaxial load is applied [6][66], it is decided to not include the normal averaging, the coplanar energy release rate and the noncoplanar energy release rate failure criterion in this thesis and focus on other more novel failure criteria for which the maximum principal stress is not the dominant criterion.

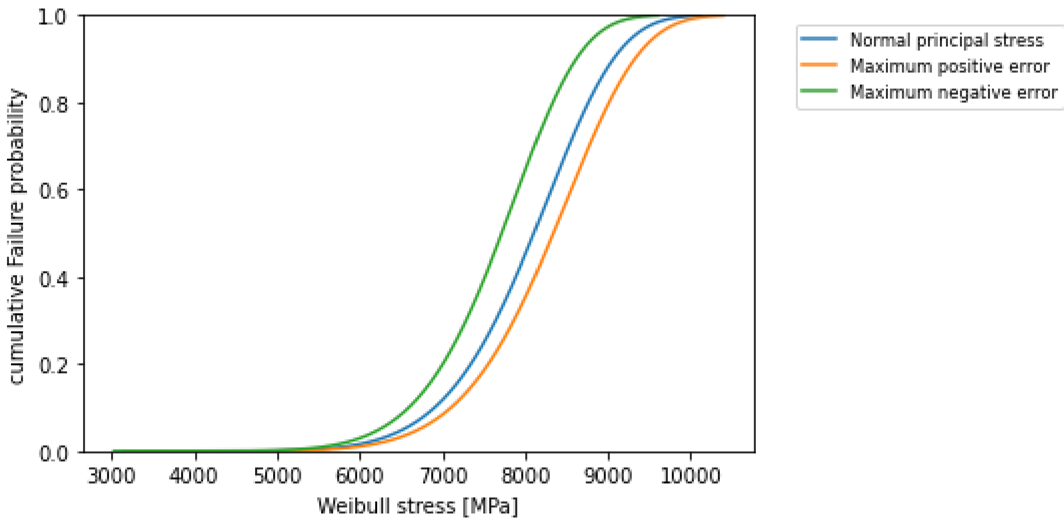


Figure 5.4: Estimation range error $K_{jc}$ values

Based on the papers of Yin [68], Beremin [9] and Testa [55], the assumption is made that the constraint, and thus the triaxiality, acting on the hard particle is very important for cleavage initiation. In this thesis the following possible methods to determine constraint are considered:

- The constraint is dependent on the triaxiality of the element in which the crack originates. As explained earlier, the assumption is made that the distribution and orientation of the hard particles in ferritic steels are random, while ferritic steel is considered as an isotropic material. This means it is likely that there will always be a micro-crack that lies in the orientation perpendicular to the maximum principal stress.

- The magnitude of the middle or minimum principal stress relative to the maximum principal stress is a good indication of the constraint around the crack tip. This means that the assumption is made that the middle principal stress influences the failure probability and is not just dependent on the maximum principal stress.

In line with the first method, the triaxiality is considered as a failure criterion. The initial idea was to create a structure similar to the principle of independent action, with the Weibull parameter $m$, being replaced by the triaxiality acting on the specimen. To study the effect of triaxiality, the level of triaxiality has to be determined first. This is done using the definition of stress triaxiality ($\eta$), where the hydrostatic stress is divided by the equivalent von Mises Stress:

$$\eta = \frac{\frac{1}{3}(\sigma_1+\sigma_2+\sigma_3)}{\frac{1}{\sqrt{2}}\sqrt{(\sigma_1-\sigma_2)^2+(\sigma_2-\sigma_3)^2+(\sigma_3-\sigma_1)^2}}. \tag{5.1}$$

The resulting failure criterion is:

$$\sigma_q = ((<\sigma_1>^{\eta}+<\sigma_2>^{\eta}+<\sigma_3>^{\eta})^{\frac{1}{\eta}}). \tag{5.2}$$

Other conditions are considered as well, in which the failure criteria is not changed. Instead the triaxiality on the small element in the mesh determines if the element is likely to fracture according to the maximum principal stress criteria or hydrostatic stress criteria. This approach leads to a number of conditions, in which <> means that only values of stress higher than 0 are considered:

$$\sigma_q = \begin{cases} <\sigma_1>, & \text{if } \eta > x \\ 0, & \text{otherwise} \end{cases} \tag{5.3}$$

$$\sigma_q = \begin{cases} \frac{(<\sigma_1>+<\sigma_2>+<\sigma_3>)}{3}, & \text{if } \eta > x \\ 0, & \text{otherwise} \end{cases} \tag{5.4}$$

$$\sigma_q = \begin{cases} <\sigma_1>, & \text{if } \eta < x \\ 0, & \text{otherwise} \end{cases} \tag{5.5}$$

$$\sigma_q = \begin{cases} \frac{(<\sigma_1>+<\sigma_2>+<\sigma_3>)}{3}, & \text{if } \eta < x \\ 0, & \text{otherwise} \end{cases} \tag{5.6}$$

$$\sigma_q = \begin{cases} <\sigma_1>, & \text{if } \eta \leq x \\ \frac{(<\sigma_1>+<\sigma_2>+<\sigma_3>)}{3}, & \text{if } \eta > x \end{cases} \tag{5.7}$$

The reasoning behind the condition in equations 5.3 and 5.4 is that only elements subjected to a significant triaxiality will experience failure. This hypothesis is tested using both the maximum principal stress and hydrostatic stress criteria. In equations 5.5 and 5.6, the opposite is considered; only elements that do not experience a significant triaxiality are used to determine the Weibull stress. Finally, a combination of the above is tested, in which the hydrostatic stress is considered if the triaxiality is larger than x, while the maximum principal stress is considered if the triaxiality is smaller than x. The largest triaxiality considered is 2.4, as observed by Jiang [61].

All of these equations rely on the assumption that the elements are the right size to make sure fracture initiation is independent of the element size, as mentioned in Chapter 2.

Another set of criteria following the second method are also considered. This method is implemented in a similar manner as the implementation of the triaxiality. The condition has been changed to include the middle principal stress or the minimum principal stress. To each of these conditions, a failure criteria is attached. Equations 5.8 and 5.9 use similar conditions, in which the constraint on the crack tip is measured as a function of the maximum and middle principal stress. If the middle principal stress is larger than a given fraction of the maximum principal stress, the hydrostatic stress is assumed to be the criteria for which elements can fail, while the maximum principal stress is considered otherwise. This assumption tests if there is a cutoff level of constraint where variations of the hydrostatic stress criteria can be used to evaluate the effect of the biaxial load on the failure probability of the specimen. Equations 5.10 and 5.11 are similar to the above equations, but evaluate if the minimum principal stress can be used in the condition instead.

$$\sigma_q = \begin{cases} \frac{(\sigma_1+\sigma_2+\sigma_3)}{3}, & \text{if } \sigma_2 > \mathrm{x}\cdot\sigma_1 \\ \sigma_1, & \text{otherwise} \end{cases} \tag{5.8}$$

$$\sigma_q = \begin{cases} \frac{(\sigma_1+\sigma_2)}{2}, & \text{if } \sigma_2 > \mathrm{x}\cdot\sigma_1 \\ \sigma_1, & \text{otherwise} \end{cases} \tag{5.9}$$

$$\sigma_q = \begin{cases} \frac{(\sigma_1+\sigma_2+\sigma_3)}{3}, & \text{if } \sigma_3 > \mathrm{x}\cdot\sigma_1 \\ \sigma_1, & \text{otherwise} \end{cases} \tag{5.10}$$

$$\sigma_q = \begin{cases} \frac{(\sigma_1+<\sigma_2>)}{2}, & \text{if } \sigma_3 > \mathrm{x}\cdot\sigma_1 \\ \sigma_1, & \text{otherwise} \end{cases} \tag{5.11}$$

Finally, equation 5.12 tests if elements that experience a large multiaxial stress propagate at all. This is implemented by removing the contribution of elements that experience a significant multiaxial loading, and assuming that if these elements do not experience such loading, the maximum principal stress criterion is sufficient.

$$\sigma_q = \begin{cases} 0, & \text{if } \sigma_2 > \mathrm{x}\cdot\sigma_1 \\ \sigma_1, & \text{otherwise} \end{cases} \tag{5.12}$$

To determine the approximate value of the value of x, for each equation, a variety of values of x has been tested. In general, values of x between zero and one are plotted to show how the failure criterion behaves.

# 6

# Results

After the calibrating process is finished, the calibrated Weibull parameters are used to construct a relationship between small and large scale yielding. Based on the provided $J_c$ values by Link [31], the critical Weibull stresses can be found for all the specimens. The resulting Weibull stresses are then plotted against the cumulative failure probability using the assumption that the value distribution scales linearly with the number of provided data points. This is best understood as the following equation:

$$\mathrm{Pf} = i/(N+1), \tag{6.1}$$

where i is the rank position of the Weibull stresses of the specimen, and N is the total number of experiments.

Using Gao's calibration method [19], the Weibull parameters are then determined by using the data from the SENB experiments, as Gao's method has been developed for these types of specimens. It should be noted that other sets are possible, as long as there is a significant difference in the level of constraint between the sets. Based on the number of single edge notched bend experiments done using the material left by the broken cruciform specimens, 35, both the slope and the mean are accurately determined. The failure probability function is then determined for each of the three stress parameters as described in Chapters 2 and 5. From the set of criteria used by Bass [66], only the maximum principal stress, hydrostatic stress and principal of independent action are considered.

## 6.1. Resulting failure distribution

The failure distributions resulting from Bass's suggestions are displayed in Figure 6.1 show that the maximum principal stress shows a relatively good agreement with the predicted failure probability, as does the principle of independent action stress criterion, while only the uniaxial specimen shows good agreement with the predicted failure probability. The biaxially loaded specimen shows a difference in results, with the Weibull distribution for the hydrostatic stress predicting larger Weibull stresses at failure than the uniaxial predicted failures. This effect is not present when the maximum principal stress criterion or principle of independent action are used, with both the maximum principal stress and the principle of independent action showing relatively good agreement with the predicted cumulative failure probability. What should also be noted is that the predicted slope is similar to the slope as predicted by all three failure probabilities.

## 6.2. The effect of triaxiality

As described in Chapter 5, there are a number of criteria that are tested to determine the effect of constraint on the determination of the Weibull stress, which were not included in the work of Bass [66]. The first set is based on the assumption that the constraint is dependent on the triaxiality of the element in which the crack originates. To that end, a few equations have been considered which only allowing elements to contribute to the Weibull stress if the triaxiality has passed a certain level. This is evaluated using equations 5.3 and 5.4 for both the maximum principal stress and hydrostatic stress criteria. For these equations the triaxiality is varied between 0 and 1.5, which is assumed to be the maximum triaxiality that will be observed [61]. Additionally, the opposite of equations 5.3 and 5.4 is tested as well, only allowing elements to contribute if the triaxiality has not passed a certain level. This is evaluated using equations 5.5 and 5.6, and again the triaxiality is varied, but

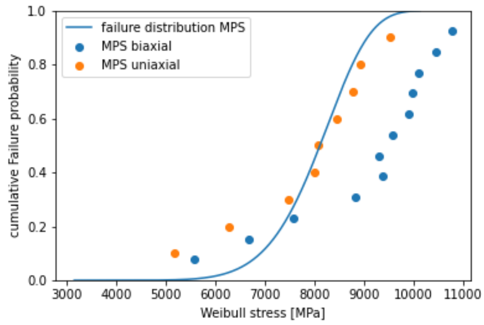


(a) Failure probability - maximum principal stress

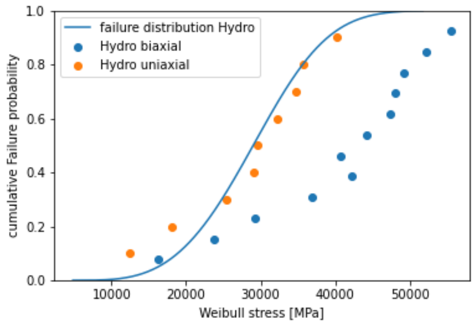


(b) Failure probability - hydrostatic stress

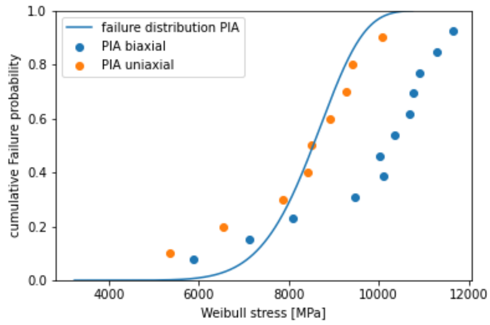


(c) Failure probability - principal independent action

Figure 6.1: plots of the failure probabilities of the maximum principal stress (a), the hydrostatic stress (b) and the principle of independent action criteria (c).

now between 1.5 and 2.4. Finally, a combination of the two approaches, as mentioned above, is considered. This approach lets elements that have significant triaxiality contribute with the hydrostatic stress criterion, while the elements that are not significantly affected by triaxiality contribute with the maximum principal stress. This is evaluated using equation 5.7.

When these criteria are used to determine the Weibull stress parameters, the results as shown in Figure 6.2 are obtained. It can be seen that from equation 5.3, if an $\eta$ of 0 is considered, the maximum principal stress criterion is obtained, while if larger values of eta are considered, the resulting biaxial prediction will start diverging from the starting maximum principal stress criterion.

If the opposite equations 5.5 and 5.6 are considered, it is observed that for large triaxialities, the original equation is obtained. When smaller cut-off triaxialities are considered, the results start to converge. Convergence is obtained around a triaxiality slightly larger than 1.7 for equation 5.5 and around a triaxiality slightly smaller than 1.6 for equation 5.6.

Finally, if equation 5.7 is considered, it is observed that the predicted failure probability curve of the biaxially loaded specimen starts diverging from the uniaxially loaded specimen when the considered triaxiality decreases. It is seen that the predicted Weibull stresses from the biaxially loaded specimen become larger than the predicted Weibull stresses by the uniaxially loaded specimen.

## 6.3. The effect of the middle principal stress

Similar to the previous section, there are a number of ways in which the effect of the second principal stress can be evaluated. For example, it is possible that the middle only start affecting the Weibull stress after a certain level of constraint has been reached. When a fraction of the maximum principal stress is equal to the middle principal stress is used as this criterion, as can be seen in equation 5.8. In the case that this fraction is one, the original hydrostatic stress criterion is recovered from equation 5.8. This can be observed in the Figures of 6.4.

From these results, it is observed that the resulting failure distribution starts matching the failure prob-

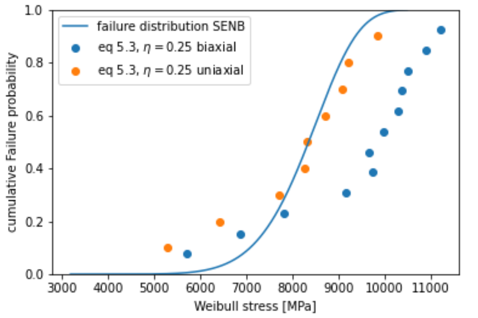


(a) Equation 5.3, $\eta = 0.25$

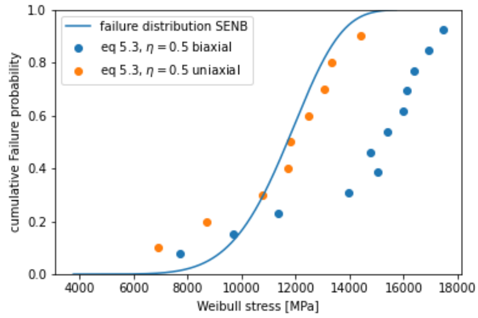


(b) Equation 5.3, $\eta = 0.5$

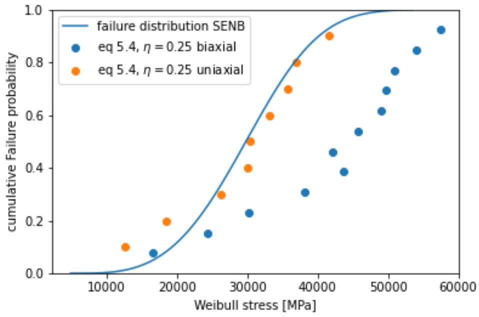


(c) Equation 5.4, $\eta = 0.25$

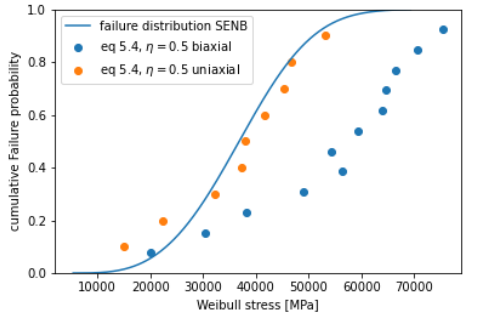


(d) Equation 5.4, $\eta = 0.5$

Figure 6.2: The predicted failure probabilities vs the found Weibull distributions for equation 5.3 and 5.3

ability as described by the SENB specimen when the fraction of the middle principal stress becomes small compared to the maximum principal stress.If the fraction becomes large, the maximum principal stress criterion is regained, as expected. It should be noted there is a large jump in results between the 0.5 and 0.75 fractions, which is not observed between the other fraction.

If the hydrostatic stress criterion is altered to only include the middle principal stress, the results as observed in the Figures of 6.6, it becomes apparent there is no significant difference between the results of equation 5.8 and 5.9.

## 6.4. The effect of the minimum principal stress

If instead of the middle principal stress, the minimum principal stress is considered as the measure of constraint, the results as shown in Figure fig:Results eq 8.8 are obtained. It is observed that the predicted biaxial failure distribution converges to the SENB failure distribution between a fraction of 0.25 and 0.5. If equation 5.11 is considered, similarly to the results from the section on the middle principal stress, it is again observed that if the fraction of the maximum principal stress is larger than chosen principal stress, the predicted failure distribution of the biaxial and uniaxial specimens does not change. However, if the fraction becomes smaller than 75%, the effect on the failure probability of the biaxial specimen becomes significant. If even smaller values are then considered, the resulting failure distribution for the biaxial specimen starts to converge to the uniaxial failure distribution.

In the case a cutoff is used, as proposed in equation 5.12, it is observed that the results show a similar shift to the results from the triaxiality condition is equation 5.5. This is seen in the Figures of 6.9. The fraction of the maximum principal stress for which there results show the best agreement is precisely $\frac{2}{3}^{rd}$. Additionally, it was observed that the calibration method becomes unstable when slightly lower fractions are considered.

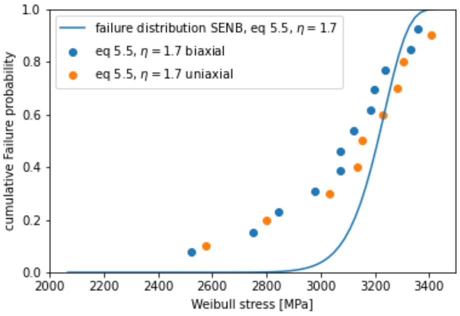


(a) Equation 5.5, $\eta = 1.7$

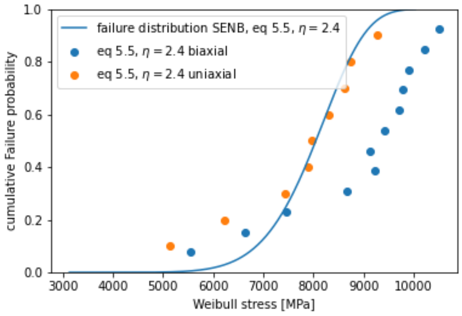


(b) Equation 5.5, $\eta = 2.4$

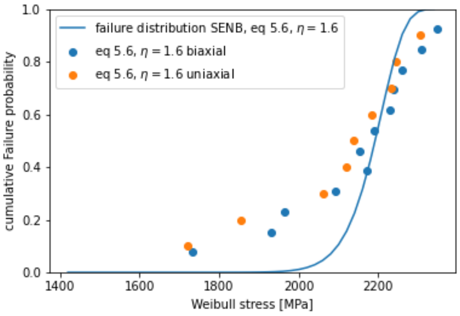


(c) Equation 5.6, $\eta = 1.6$

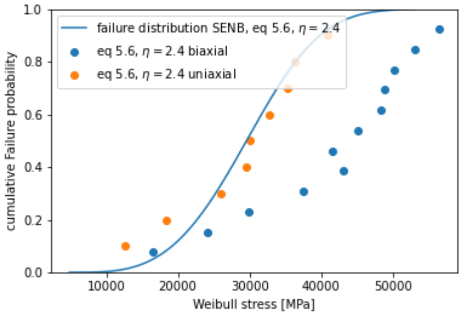


(d) Equation 5.6, $\eta = 2.4$

Figure 6.3: The predicted failure probabilities vs the found Weibull distributions for equation 5.5 and 5.6

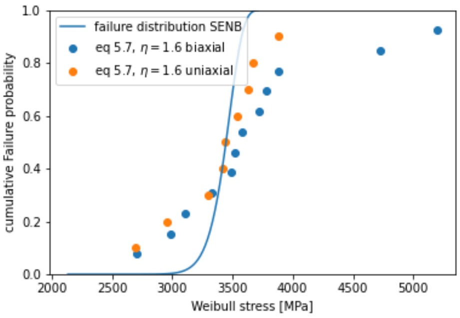


(a) Equation 5.7, $\eta = 1.6$

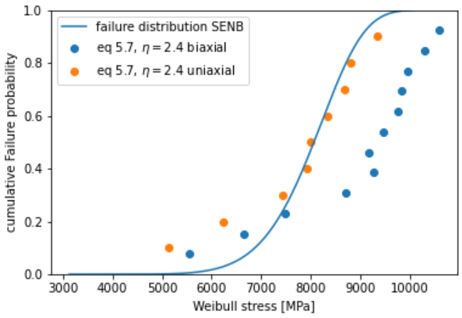


(b) Equation 5.7, $\eta = 2.4$

Figure 6.4: The predicted failure probabilities vs the found Weibull distribution for equation 5.7

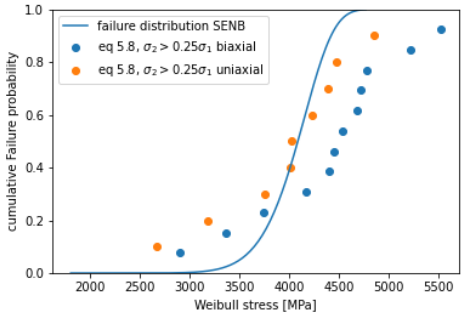


(a) Equation 5.8, $\sigma_2 < 0.25 \cdot \sigma_1$

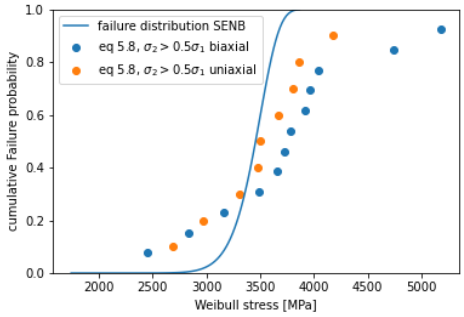


(b) Equation 5.8, $\sigma_2 < 0.5 \cdot \sigma_1$

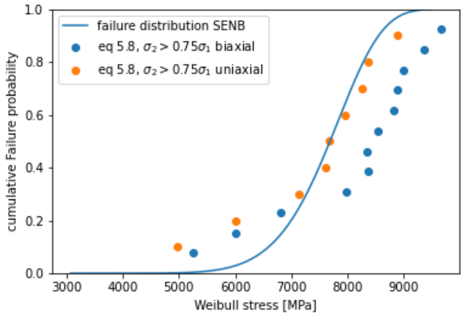


(c) Equation 5.8, $\sigma_2 < 0.75 \cdot \sigma_1$

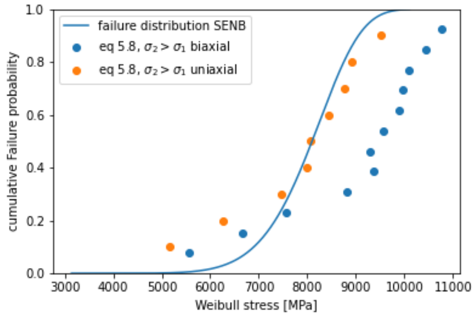


(d) Equation 5.8, $\sigma_2 < \sigma_1$

Figure 6.5: The predicted failure probabilities vs the found Weibull distributions for equation 5.8 for varying values of x

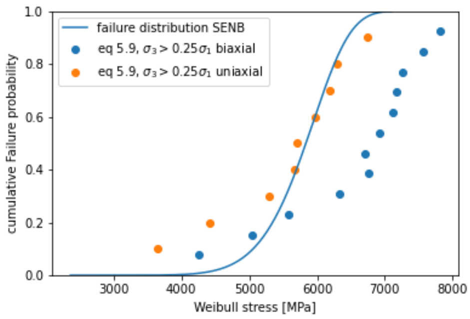


(a) Equation 5.9, $\sigma_2 < 0.25 \cdot \sigma_1$

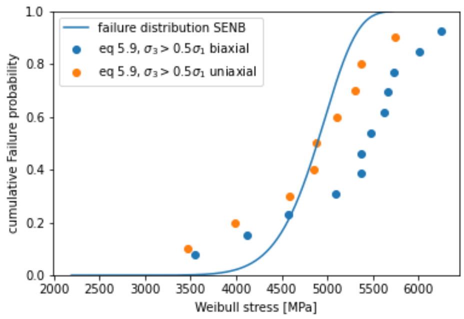


(b) Equation 5.9, $\sigma_2 < 0.5 \cdot \sigma_1$

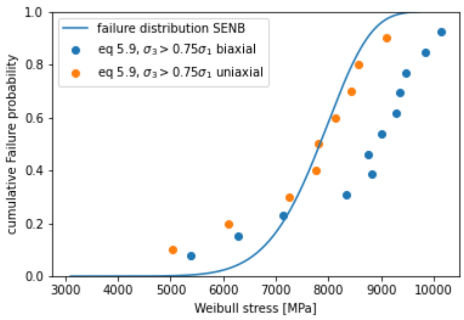


(c) Equation 5.9, $\sigma_2 < 0.75 \cdot \sigma_1$

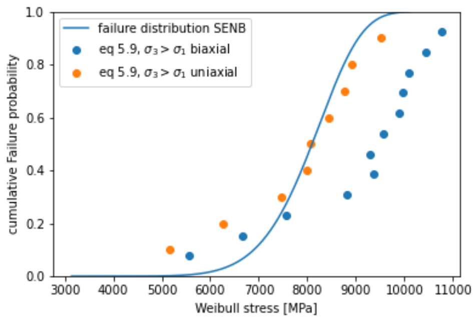


(d) Equation 5.9, $\sigma_2 < \cdot \sigma_1$

Figure 6.6: The predicted failure probabilities vs the found Weibull distributions for equation 5.9 for varying values of x

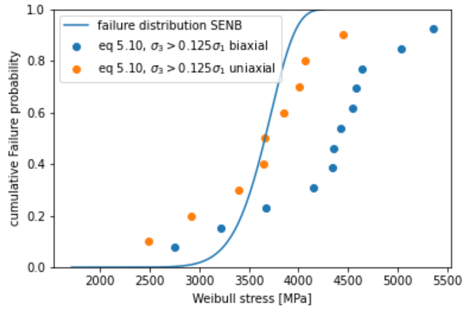


(a) Equation 5.10, $\sigma_3 < 0.125 \cdot \sigma_1$

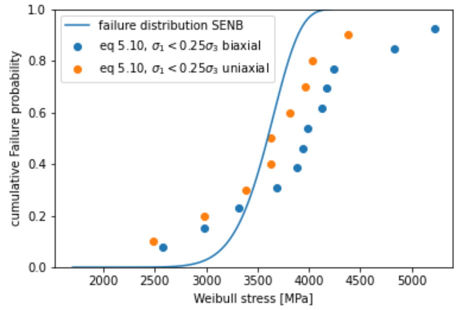


(b) Equation 5.10, $\sigma_3 < 0.25 \cdot \sigma_1$

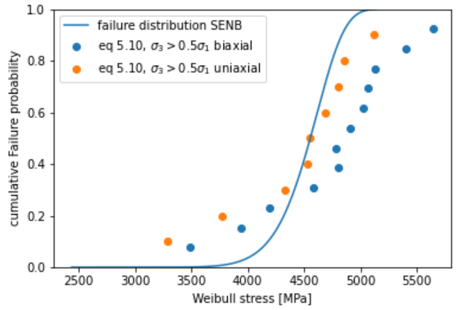


(c) Equation 5.10, $\sigma_3 < 0.5 \cdot \sigma_1$

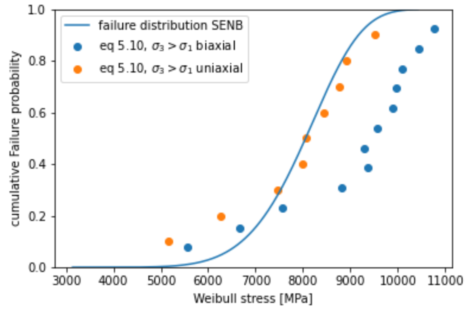


(d) Equation 5.10, $\sigma_3 < \sigma_1$

Figure 6.7: The predicted failure probabilities vs the found Weibull distributions for equation 5.10 for various levels of x

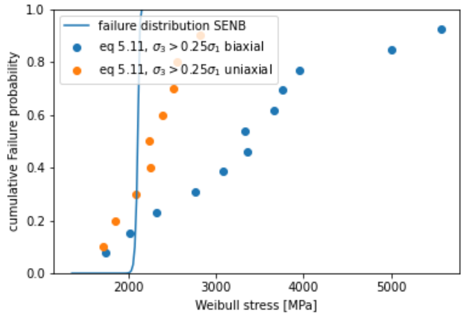


(a) Equation 5.11, $\sigma_3 < 0.125 \cdot \sigma_1$

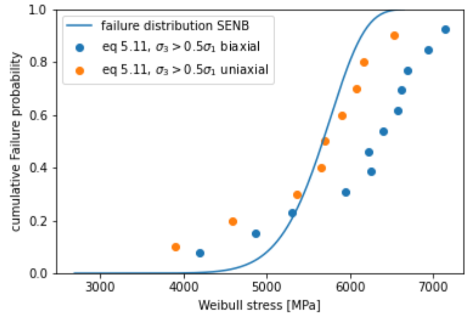


(b) Equation 5.11, $\sigma_3 < 0.25 \cdot \sigma_1$

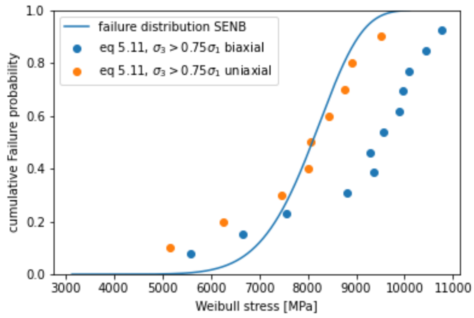


(c) Equation 5.11, $\sigma_3 < 0.5 \cdot \sigma_1$

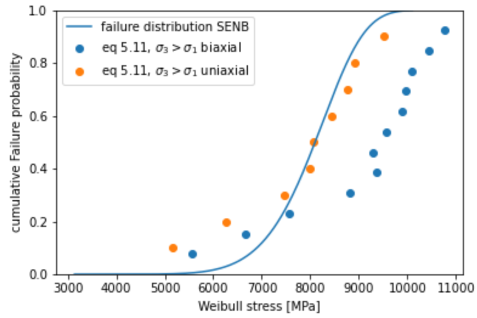


(d) Equation 5.11, $\sigma_3 < \sigma_1$

Figure 6.8: The predicted failure probabilities vs the found Weibull distributions for equation 5.11 for various levels of x

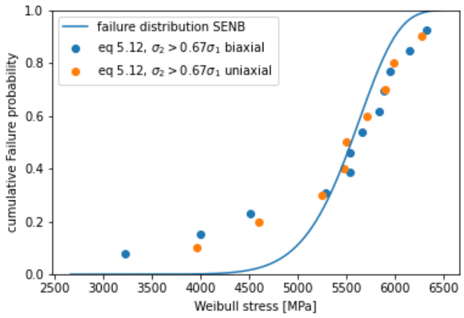


(a) Equation 5.12, $\sigma_2 < 0.67 \cdot \sigma_1$

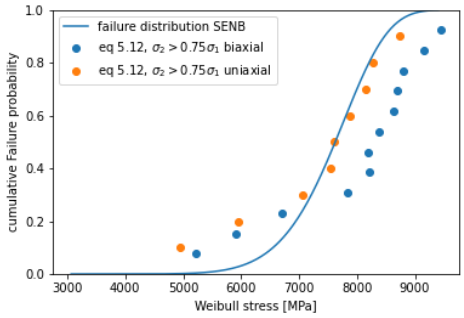


(b) Equation 5.12, $\sigma_2 < 0.75 \cdot \sigma_1$

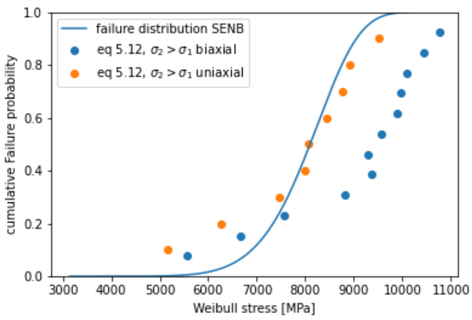


(c) Equation 5.12, $\sigma_2 < \sigma_1$

Figure 6.9: The predicted failure probabilities vs the found Weibull distributions for equation 5.12 for various levels of x

# 7

# Discussion

The results found and described in Chapter 6 are analyzed and compared to results in the work of Weibull, Yin and Link [66][68][31]. After the analysis has concluded, more elaboration on possible causes is included in the final part of the discussion.

## 7.1. Analysis results

As can be seen in the Figures of 6.1, there is a small, but clear difference between the maximum principal stress, principle of independent action and the predicted failure probability. The hydrostatic stress shows a larger difference with the failure probability for the biaxial specimens, but a relatively small difference when the uniaxial specimen is considered. This is as expected, because the biaxial loading induces higher middle and minimum principal stresses. Hence, the hydrostatic stress is found to be to be larger than when the specimen is loaded biaxially, thus leading to the result as observed in Figure 6.1.

This does not explain why the maximum principal stress and principle of independent action show a difference in distribution between the biaxial and uniaxial specimens, as the maximum principal stress criterion only takes the maximum principal stress into account and the principle of independent action ensures that the highest stresses is the most important, due to the middle and minimum principal stresses always being smaller than the maximum principal stress. Consequently, the exponent of the Weibull modulus $m$ causes the difference between the maximum and minimum principal stress to become even larger and thus when the stresses are added together and the inverse exponent is applied, only the maximum principal stress has a large effect on the resulting Weibull stress when the principle of independent action is applied. This means that the maximum principal stress criterion is effectively a form of the principle of independent action, as long as the Weibull modulus $m$ is sufficiently large and the difference between the maximum, middle and minimum principal stresses is significant. Since the result of the maximum stress criterion and the principle of independent action do not differ, it can be concluded that there is a significant difference between the maximum and middle principal stress. Additionally, the calibrated Weibull modulus $m$ is large enough to ensure the principle of independent action is converged and results in the maximum principal stress criterion.

However, it is seen that the biaxial specimens experience significantly higher Weibull stresses before failure, for both the maximum principal stress criterion, as well as the principle of independent action. This means that fracture occurs for significantly larger maximum principal stresses. Since the maximum principal stress shows good agreement with the predicted failure probability for the uniaxial specimen, while the biaxial specimen has a larger difference, it is thus clear that the constraint has a large effect on the predicted Weibull stresses.

Initially, an attempt was made to explain this result by looking the properties of the $J$-integral and how the cruciform specimen reacts to biaxial loading. As shown in chapter 2 and in the work of Rice [46], the $J$-integral is based on the energy release rate measured by taking the integral over a two dimensional surface around the crack tip. This integral is path-independent, but only for small scale yielding and proportional loading. This has been confirmed by finding that when the number of contours used by Abaqus changes, the $J$-integral tends towards convergence after a certain number of contours, as shown in Figure 4.13, for example. This indicates the $J$-integral is assumed to remain path independent by the modelling software. As mentioned in the work of Bakker [5], a three-dimensional J-integral is no longer path independent, and is thus no longer a direct measurement of the fracture toughness. Hence, the resulting fracture toughness as obtained by modelling software should be considered as an indication of the fracture toughness, not as the definite fracture toughness.

What can explain the difference in the graphs is the loss of constraint that occurs when the maximum principal stress is considered over the hydrostatic stress. As mentioned, the $J$-integral calculated over a two dimensional surface, which means that it can only take the strain in two directions into account. However, in the case of biaxial loading the principal of plane strain is no longer true, which means that the $J$-integral does not take the strain in this third dimension into account. This is also true for the reported $J$ values used to find the result. However, in the work of C. Meek[41], it has been concluded that the $J$-integral increases when biaxiality becomes larger, which is due to an increase in constraint with increasing biaxiality. This indicates that the the increase in strain due to the biaxial loading still affects the J-integral significantly. As a result, the constraint correction as used by Gao [19] will not be able to correct the toughness of biaxially loaded specimens appropriately if the failure criteria as described in Bass's paper are considered [66]. The results as shown in the Figures of 6.1 thus indicate that other failure criteria should be considered. As elaborated on in Chapter 5, the failure criteria used by Bass might not accurately represent the actual fracture in the structure. For example, the failure criteria do not evaluate the effect of triaxiality in the structure. As described in the paper by Ma [35], higher levels of triaxiality gives rise to an inverse relation between the local cleavage fracture stress and the macroscopic fracture toughness. Thus, the higher stress triaxiality can prevent cracks from propagating. Based on the observations from the results and the work of Ma [35], Meek [41] and testa [55], a new set of failure criteria is constructed, which explores the effect of triaxiality and the level of the other principal stresses.

As mentioned in the previous section, there is a clear effect of constraint on the stress criterion used; the distribution of both the hydrostatic, maximum principal stress criteria and principle of independent action show that only the uniaxially loaded specimens show good agreement with the predicted failure distribution. Similarly, there is only a small difference between the biaxial and uniaxial loading when considering the hydrostatic stress, which indicates the biaxial effect is small. Because of this, the failure criterion needs to take both multiaxial loading and constraint into account. This can be done by changing the extend to which the middle and minimum principal stresses influence the predicted Weibull stress. By implementing a cutoff where elements with high triaxiality are considered as elements in which propagation is no longer possible, the remaining elements can be used to determine the Weibull stress using the Maximum principal stress or hydrostatic stress criterion. The opposite is also considered, and can be used as a verification tool.

The method to determine the triaxiality is shown in equation 5.1, where the level of triaxiality depends on the fraction of the hydrostatic stress and von Mises stress. This led to the results as shown by the Figures of sets 6.2, 6.3 and 6.4. From these results it is found that for equations 5.3 and 5.4, indeed the resulting failure probability of the biaxially loaded specimen diverges from the initial case where all elements are considered. This indicates that elements with higher triaxiality have significantly larger cleavage fracture toughness.

If the opposite is considered, where elements are no longer considered to contribute to fracture if the cutoff is for a large triaxiality, in this case 2.4, it can be observed that the original Maximum principal and hydrostatic stress criterion are obtained. For example, equations 5.5 and 5.6 show this behaviour. If the cutoff is at a lower level of triaxiality, the resulting failure distribution start to show good agreement, before the calibration method becomes unstable when the cutoff is set even lower. The triaxiality for which the best agreement is found lies around 1.6 to 1.7.

Finally, a combination of equations 5.4 and 5.5 is also considered, in the form of equation 5.7. The behaviour of this criterion is peculiar, as for larger failure probabilities, the Weibull stress starts to diverge, while there is agreement for lower failure probabilities. This is due to the specimens that experienced higher failure probabilities also have more elements that are loaded above the cutoff triaxiality, and thus taking the hydrostatic stress in the elements with high triaxiality in these specimens into account. Hence the predicted Weibull stress increases significantly.

These results indicate that the constraint in an element does influence which stress state leads to failure. However, to get a more complete understanding of how the different principal stresses behave, the middle and minimum principal stresses are also considered. These are considered in equations 5.8 to 5.12. The results of equations 5.8 to 5.11 produce results similar to the results for equation 5.7. This makes sense, as the criteria are very similar, with the cutoff being defined as the middle principal stress instead of the triaxiality. The results show that the maximum, middle and minimum principal stress are related to each other, as is expected from simple mechanics of materials. However, since there is plasticity in front of the crack tip, a direct relationship is difficult to establish. Using Henky's equation, $\epsilon_{11} = C \cdot (\sigma_{11} - 0.5(\sigma_{22} + \sigma_{33}))$ , it is possible to relate the stresses and strains. However, since the cruciform specimen is not in plane strain, simplifying Henky's equation is not possible. Since this means the hardening coefficient C in Henky's equation has to be determined, it was decided not to pursue this approach. To still determine the stress ratio cutoff for which the biaxial and uniaxial specimens show good agreement, the ratio between the maximum and middle principle stress is considered, as in equation 5.12.

For this equation, it was observed that at a ratio of $\sigma_2 = \frac{2}{3}\sigma_1$, the biaxial and uniaxial cruciform specimen show essentially perfect agreement. Since we know the triaxiality for which the maximum principal stress equation shows good agreement, it is possible to find the ratio of $\sigma_3$ as well, which is determined to be approximately $\sigma_3 = \frac{1}{2}\sigma_1$. Essentially, the principal stress state for which the elements in the finite element model will no longer experience fracture is $\sigma_1(1, \frac{2}{3}, \frac{1}{2})$. To give physical meaning to this statement; it is observed that the middle principal stress in the elements around the crack tip is in line with the second arm of the cruciform specimen, and the maximum principal stress is line with the first arm of the cruciform specimen. From these results it can be concluded that the stress state around the crack tip has a large effect on fracture toughness.

It should be noted that the cumulative error as discussed in Chapter 5 does not significantly affect the results. In general, this error would cause the failure distribution to shift a little bit, and change its inclination. As discussed earlier, since all parts have the same material model, the error induced by the material are not visible. It should be noted that the error in the determination of the fracture toughness can affect the results. However, this error is small in comparison to the difference between the resulting fracture distribution of the uniaxially and biaxially loaded cruciform specimens.

## 7.2. The effect of the reference volume

The reference volume is only used for the purpose of this thesis, and the effect of the reference volume is self-consistent with all the results. Since a change in reference volume will have a large effect on the observed failure probability, it is important to realize that the results of this thesis might not match the results as reported in other papers. However, it is possible to convert the results of this thesis into a more general form by dividing the predicted Weibull stresses with the reference Volume [66].

# 8
# Conclusions and Recommendations

Based on the results and discussion in Chapters 6 and 7 a final conclusion is drawn, and the research question is answered. Additionally recommendations are made based on the process and availability of data.

## 8.1. Conclusion

The original research question is: *"What is a representative stress parameter that can be used to determine the distribution of the cleavage fracture toughness of ferritic steels under varying levels of constraint and multiaxial loads?"*.

Before we can answer this research question, first the subquestions are considered:

1. How can cleavage fracture toughness in ferritic steels be quantified?
2. What is the effect of constraint on fracture and how is this effect quantified?
3. Which method is best used to determine the distribution of the cleavage fracture toughness?
4. Which possible representative stress parameters should be considered?
5. Is the model that is found representative for a structure in the real world?

The first subquestion is answered in Chapter 2, which states that cleavage fracture toughness in ferritic steels can be defined by the J-integral in the case of both large and small scale yielding. This means the results as found by Link [31] are usable to define the critical fracture toughness and are used to determine the stresses in the structure when fracture occurs. However, these stresses are influenced by the level of constraint near the crack tip. In the paper of Meek [41], Östby [44] and Testa [55], it is identified that the level of constraint has an effect on the plastic deformation that guides the stresses around the crack tip. How much the stresses around the crack tip are distorted by the plastic deformation can be determined by the triaxiality, thus making the triaxiality a way to quantify the constraint around the crack tip.

To find how the stresses around the crack tip influence the probability of failure, the Beremin model can be used. This model used the maximum principal stress criteria to determine the probability of a flaw at the grain boundary cracking. However, both Meek [41] and Testa [55] suggest that triaxiality affects the cleavage fracture. This is further supported by the results in this thesis, as the original hypothesis was that the hydrostatic fracture criteria captures the effect of multiaxiality on the fracture toughness of the specimens in the cases of biaxial loading. It is also assumed that the maximum principal stress criteria will only capture the effect of uniaxial loading. However, as can be seen in the previous chapters, both the maximum principal stress and the hydrostatic do not show agreement with the results when the biaxially loaded specimen is considered. If the uniaxially loaded specimen is considered, both criteria do show good agreement with the predicted failure probability. This means that the the original hypothesis is wrong; the hydrostatic stress is not a good criteria to calculate the effect of multiaxial loads. The other stress criteria considered, the principle of independent action, gives approximately the same results as the maximum principal stress criteria. This was expected and in line with the results in the work of Bass [66].

This means none of the failure criteria proposed by Bass [66] match the predicted failure probability for the biaxially loaded specimen. Hence, additional failure probabilities are considered that find the effect of triaxiality and the middle and minimum principal stresses. From these results it is found that the triaxiality can be used to predict the failure probability. Additionally, when the middle and minimum principal stress are used to determine the conditions during cleavage fracture, the resulting calibration is significantly more stable, and shows good agreement with the predicted results. From this set of results, it is determined that if three dimensional stresses around the crack tip are considered, there are some volume elements for which the triaxiality is larger than approximately 1.7. These elements do not contribute to fracture, as when these elements are no longer considered, the fracture toughness prediction of both the maximum principal stress and hydrostatic stress show good agreement with the fracture toughness distribution of the SENB specimens. It was found that this triaxiality approximately corresponds with the following stress state $(\sigma_1, sigma_2 = \frac{2}{3}\sigma_1, sigma_3 = \frac{1}{2}\sigma_1)$.

Because of the good agreement between the predicted fracture toughness distribution and the fracture toughness distribution of the SENB specimens, equations 8.1 and 8.2 are proposed as the successor of the maximum principal stress criteria.

$$\sigma_q = \begin{cases} <\sigma_1>, & \text{if } \eta < 1.7 \\ 0, & \text{otherwise} \end{cases} \tag{8.1}$$

$$\sigma_q = \begin{cases} \sigma_1, & \text{if } 0.67 \cdot \sigma_1 < \sigma_2 \\ 0, & \text{otherwise} \end{cases} \tag{8.2}$$

These equations present conditions which have not been considered in the found literature, and indicate that the triaxiality significantly affects cleavage fracture. This conclusion matches the conclusion presented in the work of Testa [55].

## 8.2. Recommendations

To further improve on these results, some recommendations are made here. Firstly, changing equations 8.1 and 8.2 into more conventional failure criteria is recommended. While the method employed in this thesis allows quickly checking and changing the parameters in a clear and concise way, the condition should be changed to be comparable with standard failure criteria. This can be achieved by using an exponential form, for example:

$$\sigma_1 \cdot \left(\frac{1}{b^k + x}\right), \tag{8.3}$$

where b is an arbitrary number, which determines how quickly converge towards 0 occurs, while k is a function that depends on the triaxiality. Finally, the value of x is that of said triaxiality. This will simplify the failure criterion.

Further, it is recommended that more research is done on the effect of the middle principal stress on the fracture of hard particles in ferritic steels. This should eliminate the difference in results found for biaxial loading when other failure criteria than the maximum principal stress are considered. Following this approach, it is likely that a variation on equation 8.1 where the x is dependent on the triaxiality will produce an equation that can accurately predict the Weibull distribution of ferritic steels. The work on the J-Q model [52][53] can act as a guide towards such an equation. In this model, the parameter Q characterizes the constraint on the crack tip as a measure of the triaxiality. This parameter depends on the T-Stress as developed by Williams [65], which in turn depends on the stress intensity and the biaxiality ratio of the specimen. It should be noted that the J-Q approach does not describe the effect of the constraint on the stresses, it is a method to quantify constraint, similar to the triaxiality ratio used in this thesis.

Another recommendation is creating a new dataset of ferritic steel under biaxial load. Currently the datasets that can be used to determine biaxial loading are limited to a handful of papers, such as Bass and Link [66][31]. However, these datasets are generally incomplete, with stress/strain data missing for example. To ensure that the dataset contains the data required to find the Weibull stresses of a variety of failure criteria, it is important that the test is done efficiently and with a small, easily machinable specimen. A proposed specimen that satisfies the requirements for the determination of the stress intensity and is smaller than the cruciform specimen used in this thesis is shown in Appendix A.1. This new data set allows for more control over the data that is used for the Finite element model. This will remove a lot of the cumulative error from this thesis, as both the material model as used in Abaqus and the found values for $K_{Jc}$ will be more accurate. It should be noted that the crack tip itself should be determined based on the CTOD values obtained from this new dataset. As mentioned in Chapter 4, the root crack tip radius should be at least four times smaller than the observed CTOD. Another suggestion for the new dataset, is to consider the effect of strain rate and biaxiality on cleavage fracture for metals that are not cooled significantly. This was outside the scope of this thesis, but could be considered in the future.

Additionally, more consideration should be given the finite element model. This model is currently not optimized and can be much faster as well as more accurate if changes are made to the type of elements used, with the C3D8R element being replaced by the more widely used C3D20R element, which is a quadratic brick element with reduced integration points, as opposed to the linear brick element used in this thesis. It also rarely exhibits hourglassing while the C3D8R is known for problems with hourglassing, despite not being a problem in this thesis. The caveat is that contact calculations are problematic, as they are for all quadratic elements.

Furthermore, the meshing technique used around the crack tip can be improved by changing the aspect ratio of the elements close to the crack tip. Currently the aspect ratios of the elements are quite large, which can cause the model to become unstable more easily. By allowing more elements along the crack tip, the aspect ratio is improved and the elements are more stable. Similarly, a meshing technique where there is no transition between tetrahedral and hexahedral elements will improve the results. The transition can lead to unexpected results right at the contact between the tetrahedral and hexahedral elements. In this thesis this was solved by having a precise volume in which the stress state was determined, which was close to the crack tip. Using only a single type of element will prevent unexpected results due to transition areas. Again, a specimen that is easily meshable is proposed in Appendix A.1. Another big benefit of this proposed specimen is that this specimen can easily be broken under varying levels of biaxial loading; the level of triaxiality and the stress state around the crack tip can be varied significantly.

Finally, the use of the J-integral should be re-evaluated for specimens that do not experience plane strain. Given that plane strain is necessary for the J-integral to be two-dimensional and thus path independent, it is recommended to investigate if the fracture toughness can be described differently.

# Bibliography


[1] T.L. Anderson. *Fracture Mechanics, Fundamentals and applications*. Taylor Francis, Boca Raton, FL, 3 edition, 2005. ISBN 0849316561.

[2] A. Andrieu, A. Pineau, J. Besson, D. Ryckelynck, and O. Bouaziz. Beremin model: Methodology and application to the prediction of the euro toughness data set. *Engineering Fracture Mechanics*, 95:102–117, 2012.

[3] ASTM E1820-20ae1. Standard Test Method for Measurement of Fracture Toughness. Standard, ASTM International, Conshohocken, PA.

[4] ASTM E1921-20. Standard Test Method for Determination of Reference Temperature, $T_0$, for Ferritic Steels in the Transition Range. Standard, ASTM International, Conshohocken, PA.

[5] A. Bakker. *The three-dimensional J-integral: An investigation into its use for post-yield fracture safety assessment*. PhD thesis, TU Delft, November 1984.

[6] B.R. Bass, W.J. McAfee, P.T. Williams, and W.E. Pennell. Fracture assessment of shallow-flaw cruciform beams tested under uniaxial and biaxial loading conditions. *Nuclear Engineering and Design*, 188(3): 259–288, 1999.

[7] S.B. Batdorf and J.G. Crose. A statistical theory for the fracture of brittle structures subjected to nonuniform polyaxial stresses. 1974.

[8] S.E. Benzley, E. Perry, K. Merkley, B. Clark, and G. Sjaardama. A comparison of all hexagonal and all tetrahedral finite element meshes for elastic and elasto-plastic analysis. In *Proceedings, 4th international meshing roundtable*, volume 17, pages 179–191. Sandia National Laboratories Albuquerque, NM, 1995.

[9] F.M Beremin. A Local Criterion for Cleavage Fracture of a Nuclear Pressure Vessel Steel. Technical report.

[10] I. Calimanescum. Fatigue comparative study of a gear transmission by using finite elements analysys.

[11] J. Chen and R. Cao. *Micromechanism of cleavage fracture of metals: a comprehensive microphysical model for cleavage cracking in metals*. Butterworth-Heinemann, 2014.

[12] G.P. Cherepanov. The propagation of cracks in a continuous medium. *Journal of Applied Mathematics and Mechanics*, 31(3):503—512, Jan 1967.

[13] D.A. Curry and J.F. Knott. Effects of microstructure on cleavage fracture stress in steel. *Metal Science*, 12 (11):511–514, 1978.

[14] L.J.M.G. Dortmans, T.h. Thiemeier, A. Brückner-Foit, and J. Smart. Welfep: a round robin for weakest-link finite element postprocessors. *Journal of the European Ceramic Society*, 11(1):17–22, 1993.

[15] B. Epstein. Statistical aspects of fracture problems. *Journal of Applied Physics*, 19(2):140–147, 1948.

[16] A.G. Evans. A general approach for the statistical analysis of multiaxial fracture. *Journal of the American Ceramic Society*, 61(7-8):302–308, 1978.

[17] A.G. Evans. Statistical aspects of cleavage fracture in steel. *Metallurgical Transactions A*, 14(7):1349–1355, 1983.

[18] A.M. Freudenthal. Statistical approach to brittle fracture. *Fracture, An Advanced Treatise, II*, pages 591–619, 1968.

[19] X. Gao, C. Ruggieri, and R.H. Dodds. Calibration of Weibull stress parameters using fracture toughness data. *International Journal of Fracture*, 92:175–200, 1998.

[20] C.R. Goyal. *Uncertainty Quantification in non-linear seismic wave propagation*. PhD thesis, Carleton University, 2017.

[21] A.A. Griffith. The phenomena of rupture and flow in solids. *Philosophical transactions of the royal society of london. Series A, containing papers of a mathematical or physical character*, 221(582-593):163–198, 1921.

[22] J. Heerens and D. Hellmann. Development of the euro fracture toughness dataset. *Engineering Fracture Mechanics*, 69(4):421–449, 2002.

[23] J. Heerens and D.T. Read. Fracture behavior of a pressure vessel steel in the ductile-to-brittle transition region. 1988.

[24] T.K. Hellen and W.S. Blackburn. The calculation of stress intensity factors for combined tensile and shear loading. *International Journal of Fracture*, 11(4):605–617, 1975.

[25] J.W. Hutchinson. Singular behaviour at the end of a tensile crack in a hardening material. *Journal of the Mechanics and Physics of Solids*, 16(1):13–31, 1968.

[26] M. Janssen, J. Zuidema, and R. Wanhill. *Fracture Mechanics*. VSSD, Delft, 2 edition, 2002. ISBN 90-407-2221-8. URL `http://www.vssd.nl/hlf/m004.htm`.

[27] J.A. Joyce, R.E. Link, and J. Gaies. Evaluation of the effect of biaxial loading on the t o reference temperature using a cruciform specimen geometry. *Journal of ASTM International*, 2(1):1–18, 2005.

[28] J. Lamon and A.G. EVANS. Statistical analysis of bending strengths for brittle solids: a multiaxial fracture problem. *Journal of the American Ceramic Society*, 66(3):177–182, 1983.

[29] T. Lin, A.G. Evans, and R.O. Ritchie. A statistical model of brittle fracture by transgranular cleavage. *Journal of the Mechanics and Physics of Solids*, 34(5):477–497, 1986.

[30] R. Link. private communication, 5 2020.

[31] R.E. Link, J.A. Joyce, and C. Roe. An experimental investigation of the effect of biaxial loading on the master curve transition temperature in rpv steels. *Engineering fracture mechanics*, 74(17):2824–2843, 2007.

[32] A.E.H. Love. *A treatise on the mathematical theory of elasticity*. Cambridge university press, 2013.

[33] J.R. Low. Relation of properties to microstructure, 1954. *ASM International, Materials Park, Ohio). Google Scholar*, pages 163–168.

[34] S. M. *Fitness for Service, API 579-1/ASME FFS-1*. API Publishing, United States, 2007.

[35] H. Ma. The effect of stress triaxiality on the local cleavage fracture stress in a granular bainitic weld metal. Technical report, 1998.

[36] H. Ma. The effect of stress triaxiality on the local cleavage fracture stress in a granular bainitic weld metal. *International journal of fracture*, 89(2):143–158, 1998.

[37] Y.G. Matvienko. The effect of crack-tip constraint in some problems of fracture mechanics. *Engineering Failure Analysis*, 110:104413, 2020.

[38] F.A. McClintock and A.S. Argon. Mechanical behavior of materials. 1966.

[39] C.J. McMahon Jr and M. Cohen. Initiation of cleavage in polycrystalline iron. *Acta Metallurgica*, 13(6): 591–604, 1965.

[40] R.M. McMeeking. Finite deformation analysis of crack-tip opening in elastic-plastic materials and implications for fracture. *Journal of the Mechanics and Physics of Solids*, 25(5):357–381, 1977.

[41] C. Meek. *The Influence of Biaxial Loading on the Assessment of Structures with Defects*. The University of Manchester (United Kingdom), 2017.

[42] F. Minami, A. Brückner-Foit, D. Munz, and B. Trolldenier. Estimation procedure for the weibull parameters used in the local approach. *International journal of fracture*, 54(3):197–210, 1992.

[43] N.P. O'Dowd, Y. Lei, and E.P. Busso. Prediction of cleavage failure probabilities using the weibull stress. *Engineering Fracture Mechanics*, 67(2):87–100, 2000.

[44] E. Østby and A.O. Hellesvik. Large-scale experimental investigation of the effect of biaxial loading on the deformation capacity of pipes with defects. *International Journal of Pressure Vessels and Piping*, 85(11): 814–824, 2008.

[45] W.S. Owen, B.L. Averbach, and M. Cohen. Brittle fracture of mild steel in tension at-196 c. Technical report, MASSACHUSETTS INST OF TECH CAMBRIDGE, 1957.

[46] J.R. Rice. A path independent integral and the approximate analysis of strain concentration by notches and cracks. *J. Appl. Mech.*, 35:379–386, Jun 1968.

[47] J.R. Rice and G.F. Rosengren. Plane strain deformation near a crack tip in a power-law hardening material. *Journal of the Mechanics and Physics of Solids*, 16(1):1–12, 1968.

[48] R.O. Ritchie, J.F. Knott, and J.R. Rice. Relationship between critical tensile stress and fracture toughness in mild steel. Technical report, Brown Univ., Providence, RI (USA). Div. of Engineering, 1973.

[49] C. Ruggieri and R. H. Dodds. A local approach to cleavage fracture modeling: An overview of progress and challenges for engineering applications. *Engineering Fracture Mechanics*, 187:381–403, 2018.

[50] C. Ruggieri and R.H. Dodds. Numerical evaluation of probabilistic fracture parameters using wstress. *Engineering computations*, 1998.

[51] C. Ruggieri and R.H. Dodds. An engineering methodology for constraint corrections of elastic-plastic fracture toughness - Part I: A review on probabilistic models and exploration of plastic strain effects. *Engineering Fracture Mechanics*, 134:368–390, jan 2015. ISSN 00137944. doi: 10.1016/j.engfracmech.2014.12.015.

[52] C.F. Shih and N.P. O'Dowd. Family of crack-tip fields characterized by a triaxiality parameter—i. structure of fields. *Journal of the Mechanics and Physics of Solids*, 39(8):989–1015, 1991.

[53] C.F. Shih, N.P. O'Dowd, and M.T. Kirk. A framework for quantifying crack tip constraint. In *Constraint effects in fracture*. ASTM International, 1993.

[54] Andrew J Slifka, Elizabeth S Drexler, Douglas G Stalheim, Robert L Amaro, Damian S Lauria, April E Stevenson, and Louis E Hayden. The effect of microstructure on the hydrogen-assisted fatigue of pipeline steels. In *Pressure Vessels and Piping Conference*, volume 55713, page V06BT06A009. American Society of Mechanical Engineers, 2013.

[55] G. Testa, N. Bonora, A. Ruggiero, G. Iannitti, and D. Gentile. Stress triaxiality effect on void nucleation in ductile metals. *Fatigue & Fracture of Engineering Materials & Structures*, 43(7):1473–1486, 2020.

[56] T.J. Theiss and J.W. Bryson. Influence of crack depth on the fracture toughness of reactor pressure vessel steel. In *Constraint Effects in Fracture*. ASTM International, 1993.

[57] Unknown. Abaqus/cae user's guide.

[58] Unknown. Modes i, ii, and iii, (accessed Juli 17, 2020). URL `https://www.fracturemechanics.org/modes123.html`.

[59] journal=Engineering Fracture Mechanics volume=22 number=1 pages=149–163 year=1985 publisher=Elsevier Wallin, K. The size effect in kicresults.

[60] K. Wallin. The scatter in kic-results. *Engineering fracture mechanics*, 19(6):1085–1093, 1984.

[61] C.L. Walters and Q. Jiang. private communication, 5 2020.

[62] J. Watanabe, T. Iwadate, Y. Tanaka, T. Yokobori, and K. Ando. Fracture toughness in the transition region. *Engineering Fracture Mechanics*, 28(5-6):589–600, 1987.

[63] W. Weibull. A statistical theory of strength of materials. *IVB-Handl.*, 1939.

[64] H.M. Westergaard. Bearing pressures and cracks. *Trans AIME, J. Appl. Mech.*, 6:49–53, 1939.

[65] M. Williams. On the stress distribution at the base of a stationary crack., 1957.

[66] P.T. Williams, R. Bass, and W.J. McAfee. Shallow flaws under biaxial loading conditions-part II: Application of a weibull stress analysis of the cruciform bend specimen using a hydrostatic stress criterion. *Journal of Pressure Vessel Technology, Transactions of the ASME*, 123(1):25–31, 2001. ISSN 15288978. doi: 10.1115/1.1344235.

[67] S. Yang, Y.J. Chao, and M.A. Sutton. Higher order asymptotic crack tip fields in a power-law hardening material. *Engineering Fracture Mechanics*, 45(1):1–20, 1993.

[68] S. Yin, R. Bass, P. Williams, M. Ludwig, and E. Keim. Effect of shallow flaws and biaxial loading on transition temperatures using a weibull stress model. In *ASME Pressure Vessels and Piping Conference*, volume 46700, pages 77–84, 2004.

# Appendices

# A
# Appendix

## A.1. Appendix A

This document is made to show how and why the experiment setup was designed as it was, and shows that the experiment will behave as expected.

In order to do this, this document has three parts:

- The first shows the dimensions chosen for the parts of the experiment and demonstrates that the complete experiment fits in the testing machine.
- The second deals with the analytical analysis of the Stress intensity in front of the crack tip, and how this affects the chosen dimensions.
- The third deals with the FEM simulation using abaqus, and how the results show that the experiment behaves as intended for both Tensile and torsional loading. By intended it is meant that cleavage fracture occurs under SSY and no yielding occurs elsewhere in the experiment setup.

**Dimensions and fitting**

The experiment will be conducted using a Temperature chamber made by Innstron, of the 3119-6110 series, which has a temperature rating of -150°C to 350°C. Given that earlier testing with S690QL by Virginia was done under ambient temperatures of -130°C inside the chamber, this temperature chamber is sufficient for this experiment. This ambient temperature was needed for the steel to cool down to -100°C, as mentioned in private discussion with Ton Riemslag. The dimensions of this chamber are given in Figure A.1, which means that the length of the extensions must be lower than 657 mm :

The dimensions for the specimen and extensions are shown in Figure 1 and 2 respectively.

A pin with a diameter of 8 mm with a length of 40 mm is used to connect the specimen with the extension.

The material to be used for these parts is Stainless steel grade 316 for the extension, while the specimens are created using the S690QL material as used by Virginia.

**Analytical analysis**

To estimate the applied load under which cleavage fracture will occur, the data provided by Quanxin and Virginia for their CTOD tests of S690QL will be used. In this case, the advice was given to use material of the upper quarters of the steel, in the L-T direction. The assumption is made that, even if the material properties are different under -100°C, the material properties of S690QL and Stainless steel will behave similarly under the influence of the cryogenic temperatures. This allows us to use material properties from room temperature.

The maximum CTOD in this case was 0.077 mm, which corresponds to a maximum $K_{Ic}$ of 104 $MPa\sqrt{m}$, using the known formula:

$$\delta = \frac{K_I^2}{\frac{m\sigma E\gamma}{(1-\nu^2)}} \tag{A.1}$$

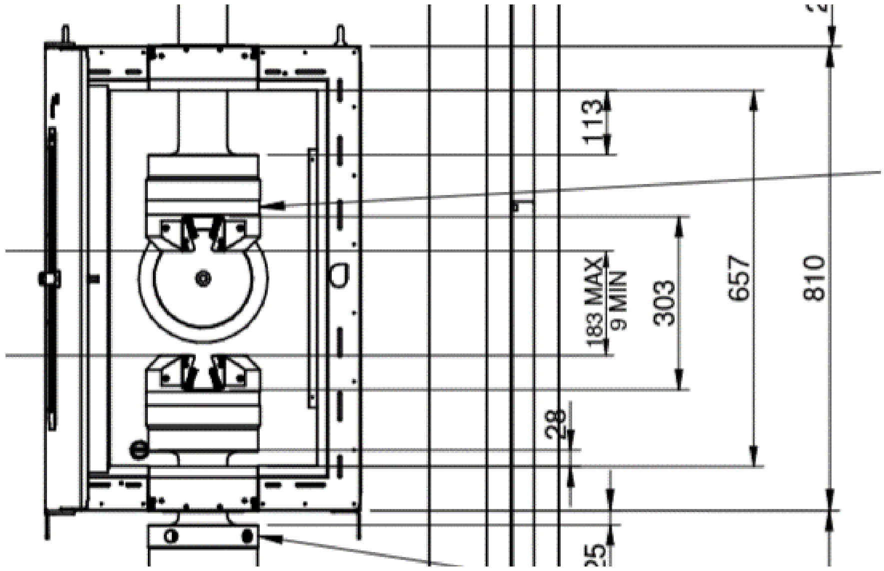


Figure A.1: Dimensions Temperature chamber

as the fracture toughness is determined assuming plane strain close to the crack, and it is known that S690QL has a yield stress of 650 MPa and a Poisson's ratio of 0.29, with a young's modulus of 200 GPa.

The load that has to be applied to get a $K_{Ic}$ of 104 $MPa\sqrt{m}$ is calculated using the formula in the book Fracture mechanics and the formula in the stress analysis of cracks handbooks, respectively being

$$K_I = 0.526P\sqrt{\frac{D}{d^2}} \tag{A.2}$$

with D being the diameter of the bar and the d being the diameter of the cross-section at the notch, and:

$$K_I = \sigma\sqrt{\pi c}\cdot F(\frac{c}{b}) \tag{A.3}$$

with $\sigma = \frac{P}{\pi b^2}$ and $F(c/b) = \frac{1}{(1-c/b)^{3/2}}[1.122 - 1.302(c/b) + 0.998(c/b)^2 - 0.308(c/b)^3]$

In this case, c and b are the crack depth and the diameter of the specimen respectively. The results of both equations are relatively close together, being 23.0 and 22.3 kN respectively. To be conservative, the load of 23 kN was chosen.

**Finite element simulation**

This section shows that the load chain of the experiment will behave as expected. It consists of two parts, the tensile simulation and the torsional simulation, considered in that order. Since the experiment will be loaded in combinations of tension and torsion, the simulation looks at the pure tension and pure torsion condition, as these conditions are assumed to be the most severe cases of loading. This means that variations of tension and torsion are assumed to be less impactful on the behaviour of the extension and the pinned connection in the specimen than the extreme cases of pure tension and pure torsion.

**Tensile load simulation**

The model was created as follows. The pin was modelled as a discrete rigid body, making the assumption that the pin will be a very strong material of our choosing, most likely a type of stainless steel. In its reference point, only 1 D.O.F. was specified, which was in the direction of the applied force. A force of 23 kN was then applied in the center of the pin. The direction of this force was in the axis of the specimen/extension and oriented to load the load chain in tension.

The extension was modelled as a deformable three-dimensional body, and on the top the extension is given 0 D.O.F.. The same thing is done for the specimen.

This pin was brought in contact with the extension and specimen, for which two separate models were created. A frictionless contact was chosen as no sliding will occur, thus making a frictionless contact accurate.

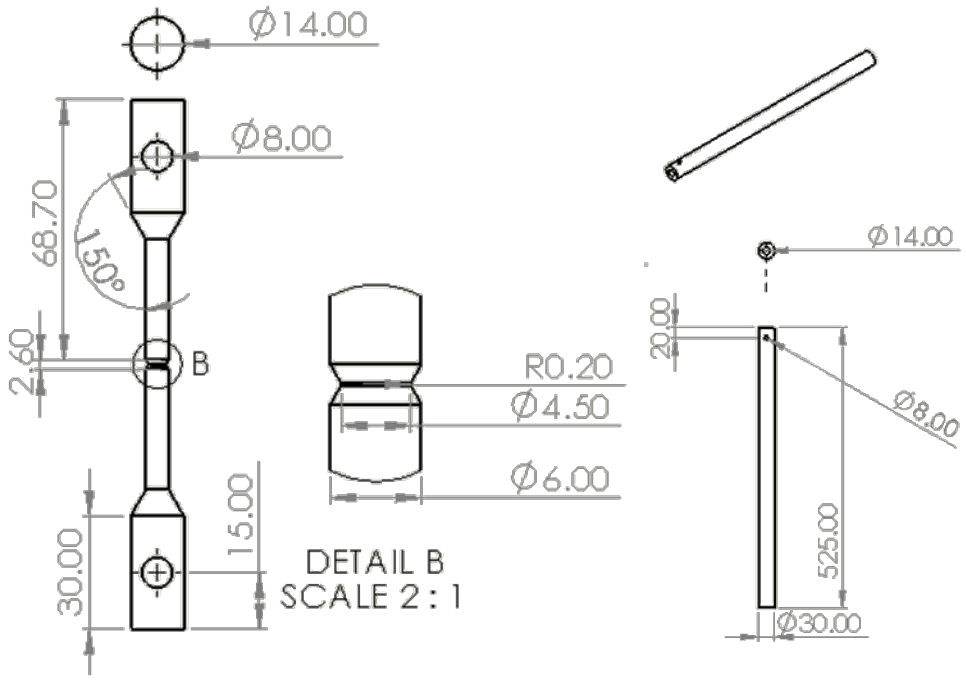


Figure A.2: Dimensions specimen and extension

**Results Tensile load simulation**

This led to the following results for the extension, in which the maximum von Mises stress is found to be larger than the yield stress. Despite the occurrence of yielding, this small deformation should not cause the pin to be stuck in the extension. This means the extension will work as intended even if the maximum possible force is applied.

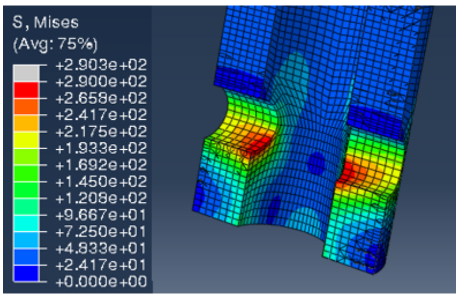


Figure A.3: Simulation results extension in tension

For the specimen, similar results are obtained, with very slight plastic deformation at the point where the stress concentration is located. Given that this only leads to a slightly larger hole, the pin should still be easy to get out. To that end there is some open space between the specimen and pin. Thus, fracture should not occur at the pinned connection between the specimen and the extension.

Finally, the applied load on the pin is considered. Using the loads applied on the pin as given by simulation an analytical method was used. The shear stress was calculated using the standard formula $\tau = \frac{2P}{\pi D_p^2}$

Then this shear stress was put into the the von Mises criteria. Applying a load of 23 kN, this von Mises stress becomes approximately 400 MPa. This indicated that the von Mises stresses would become too large when a stainless steel pin is used, but would be okay if an S690ql pin was used. To further verify this assumption, a finite element simulation of the pin was made. This simulation was the reverse of the previous two experiments, with the extension and specimen being modelled as rigid and the pin as deformable. The extension was placed under 0 D.O.F. and the Pin and specimen under 1 D.O.F., which was the direction of the applied force. The force of 23 kN was applied on the rigid specimen, similar to previous simulations.

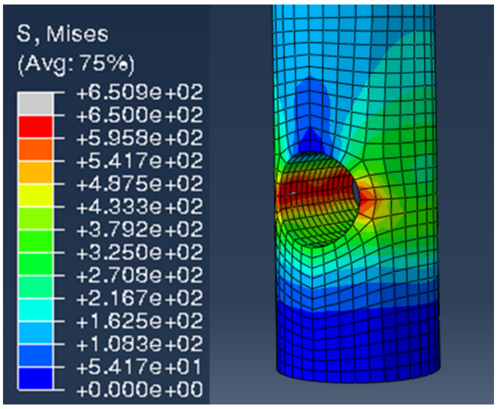


Figure A.4: Simulation results specimen in tension

A stainless steel Pin would be insufficient and deform plastically, while the S690QL pin would not deform plastically, as can be seen in the following pictures. The highest stress in the pin is found to be 605 MPa, which indicates a very strong material is needed if S690QL is not available to make this pin. The highest stress on the surface of the pin was around 400 MPa, which perfectly matches the analytical results for the average shear stress.

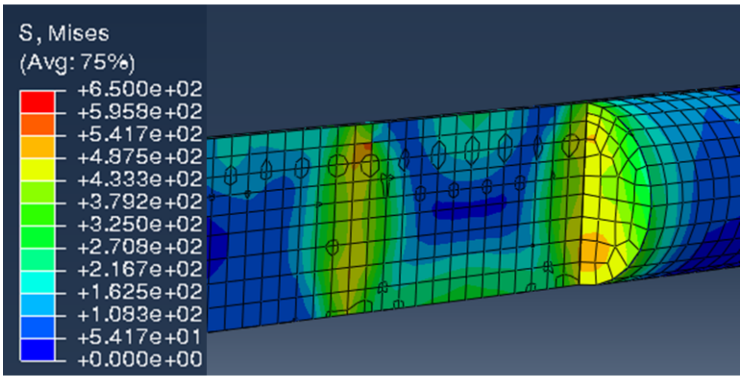


Figure A.5: Simulation results Pin in tension

**The moment simulation**

Similar to the tensile simulations, but the single D.O.F. on the pin is replaced is changed from a direction into rotation around the axis of the applied moment. This is true for both simulations. No further settings have been changed. The applied moment when fracture will occur is determined from another simulation, in which a 3 mm diameter S690QL cylinder is deformed plastically until UTS is reached. This allows us to check for the maximum possible moment to be applied before failure, assuming no weak points. To model plasticity, a simple model was used in Abaqus, using only two points. The first is at 650 MPa and has a plastic strain of 0, while the other is at 950 MPa and has a plastic strain of 0.1. The simulations was constrained by applying 0 D.O.F. on one end of the cylinder, while an increasing moment was applied on the other side.

By using 4 timesteps, each with 1 Nm addition, it was found that a moment of 3.75 Nm would lead to UTS in the cylinder using the von Mises stress criterion and, assuming equivalency, cleavage fracture in the pin. Consider that the cylinder is modelled without flaws, while in the actual specimen there will be a sharp crack tip. In front of the crack tip there will be a stress concentration, and thus the applied moment that leads to fracture is likely overestimated in the case where no flaws are considered. Hence, it can be assumed that the found moment will lead to cleavage fracture. However, it is likely that the moment that will lead to cleavage fracture is lower than the applied moment as determined by this simulation, since there are no flaws where stress concentrations could occur.

The moment was also found analytically, but this moment was not used since the analytical model does not take plastic deformation into account. If plastic deformation is not taken into account, the analytical model predicts the UTS would be reached at an applied moment of 1.5 Nm, which is significantly lower than the moment found by the simulation. This leads to the usage of 3.75 Nm as the applied torsion, as this is a conservative estimate.

**The moment simulations**

The results for the extension are very clear, for a torsional load of 3.75 Nm there are no von Mises stresses larger than 24 MPa, with the largest being approximately 10 MPa. This means that no yielding will occur when the specimen fractures under a torsional load.

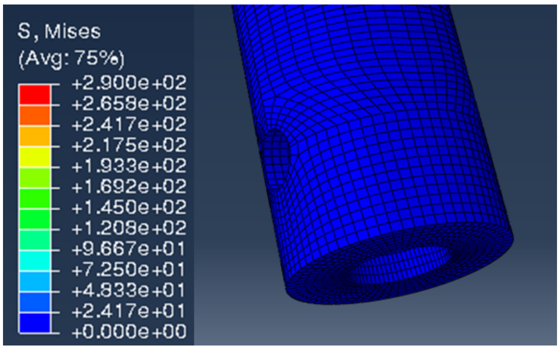


Figure A.6: Simulation results extension in torsion

The results for the specimen are clear as well. The maximum von Mises stresses are larger, but when compared to the yield stress of the S690QL specimen still much lower than yielding. This means that fracture is quite certain to occur at the notch.

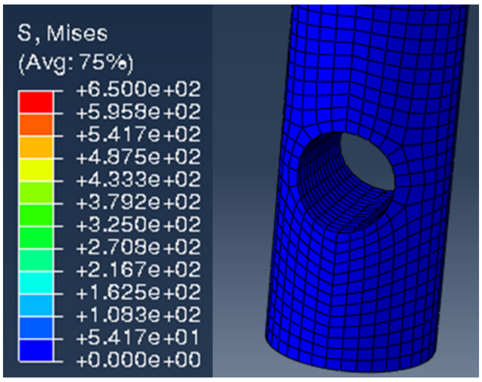


Figure A.7: Simulation results specimen in torsion

Given that the moment applies significantly lower loads on the pin, the previous calculation for the pin is assumed to be sufficient and an S690QL pin will be able to withstand this load.

Hence, it is demonstrated that the experiment will likely not behave in a way that will impact results from the crack at the notch tip. Furthermore, no plasticity will occur that prevents the setup from being unable to come apart. Finally, assuming that the superposition principle works, the stresses that occur in combinations of tension and torsion will be lower than the extreme case of pure tension. The effect of the moment on the load chain is low, which is due to the moment being dependant on the polar polar second moment of area. This area moment is very small due to the small diameter of area between the cracks in the specimen.

**Final conclusion**

Thus, the extension will be made using stainless steel of grade S316. The Specimen and Pin will both be made using S690QL, assuming this is allowed. The dimensions are as mentioned in the introduction. Finally, it is shown that it is likely that combinations of tension and torsion are less severe on the fracture of the extension and the pinned connection of the specimen.